



# Modelling nonlinearity of guided ultrasonic waves in fatigued materials using a nonlinear local interaction simulation approach and a spring model

Rafal Radecki<sup>a,b,\*</sup>, Zhongqing Su<sup>a</sup>, Li Cheng<sup>a</sup>, Pawel Packo<sup>b</sup>, Wieslaw J. Staszewski<sup>b</sup>

<sup>a</sup> Department of Mechanical Engineering, The Hong Kong Polytechnic University, Hung Hom, Kowloon, Hong Kong Special Administrative Region

<sup>b</sup> Department of Robotics and Mechatronics, AGH University of Science and Technology, Al. Mickiewicza 30, 30-059 Krakow, Poland

## ARTICLE INFO

### Article history:

Received 21 June 2017

Received in revised form 29 September 2017

Accepted 13 November 2017

Available online 16 November 2017

### Keywords:

Wave propagation

Lamb waves

Nonlinear material

Nonlinearity of guided waves

Nonlinear Local Interaction Simulation

Approach (NL-LISA)

Spring Model (SM)

Fatigue crack

## ABSTRACT

Modelling and numerical simulation – based on the framework of the Local Interaction Simulation Approach – was developed to have more insight into nonlinear attributes of guided ultrasonic waves propagating in fatigued metallic materials. Various sources of nonlinearity were considered in this modelling work, with particular emphases on higher-order harmonic generation and accumulation of nonlinearity along wave propagation. The material hyper-elasticity was considered in the model using an energy density approach based on the Landau–Lifshitz formulation; and the “breathing” motion pattern of a fatigue crack in the material was interrogated using a spring model. Upon the successful validation with the model prepared in the commercial software based on the Finite Element Methods, two scenarios were comparatively investigated, i.e. the lower and higher frequency regime. In the first case propagation of a basic symmetric mode pair was simulated using the model to observe a cumulative characteristic of the second harmonic mode with nonlinear hyper-elastic material definition upon appropriate selection of excitation frequency. In the second case, the higher-order symmetric mode pair was excited according to the “internal resonance” conditions, revealing a strong dependence of manifested nonlinearity on numerical parameters. Moreover, it was shown that with the use of the wave from the low frequency regime it was easier to differentiate later stages of the crack development, being in contrary to waves in the high frequency regime, which allowed to clearly observe early stages of the crack expansion. Such outcome lays the foundation to develop the damage detection and monitoring scheme in the field of Structural Health Monitoring based on utilising the nonlinear features of guided ultrasonic waves.

© 2017 Elsevier B.V. All rights reserved.

## 1. Introduction

Nonlinear attributes of Guided Ultrasonic Waves (GUWs) have been studied intensively for the past few years. The highly anticipated advantage of nonlinear features over their linear [1] counterparts relates in particular to their exceptionally high sensitivity to the presence of small-sized damage [2] and micro-changes in the structural material properties [3,4]. This advantage can lead to the development of new Non-Destructive Evaluation (NDE) and Structural Health Monitoring (SHM) methods suitable for the detection of damage at its embryo stage, i.e. fatigue cracks which have not yet reached a perceptible degree. When GUWs are generated at specific frequencies and traverse an elastic medium, they intrinsically interact with various nonlinear sources featured by

\* Corresponding author at: Department of Robotics and Mechatronics, AGH University of Science and Technology, Al. Mickiewicza 30, 30-059 Krakow, Poland.  
E-mail address: [rafal.radecki@agh.edu.pl](mailto:rafal.radecki@agh.edu.pl) (R. Radecki).

the medium, i.e. fatigue cracks [2,5–7], de-bonding at adhesive joints [8–10], plastic zones of material [11–13], or material nonlinearity of the medium [4,14]. Such interactions result in the distortion of the probing GUWs, shifting the wave energy from the excitation frequency to the other different frequencies. Notably, both material nonlinearity of the medium and the fatigue damage are responsible for the majority of nonlinearities manifested in captured GUW signals. Under cyclic loads, progressive degradation of the medium or deterioration of damage in the medium further intensifies these nonlinearities.

With such a premise, a diversity of NDE and SHM approaches have been developed and deployed, represented by those using high- [15–17] or sub- [18] harmonics, mixed frequency responses [19] (e.g. nonlinear wave modulation spectroscopy), shift of resonance frequency [20] (e.g. nonlinear resonant ultrasound spectroscopy), nonlinear surface waves [21,22], dual frequency mixing [23], or time reversal [24]. All above-mentioned methods have been surveyed comprehensively in [25]. The higher-order

harmonic generation, i.e. a spectral feature of GUW signals has evidenced as energy transfer from the fundamental (excitation) frequency  $\omega_0$  to the integer multipliers of the fundamental frequency ( $2\omega_0, 3\omega_0$  and so on). Amongst these higher-order harmonics, the second harmonic has been most widely exploited due to its relative convenience and feasibility in acquisition as compared with the other higher order counterparts.

There is a rich body of literature dedicated to understanding and exploiting nonlinear attributes of GUWs. This includes theoretical derivation [4,26–29], numerical modelling and simulation [14,30–33], as well as experimental validation [34–37]. Cost-effectiveness of numerical simulation has gained an increased interest and preference in these investigations. Recent studies demonstrate that the burgeoning Local Interaction Simulation Approach (LISA) [30,38–47] offers promising capabilities to model accurately and efficiently propagation of GUWs. The LISA was first introduced in the early 1990s to model the wave propagation in media with linear material properties [38–40]. With its governing equations based on a Finite Difference (FD) approximation and a top-down modelling strategy, the computational capacity of LISA is not restricted by the complexity of geometry or material properties (e.g. heterogeneous, anisotropic and nonlinear materials with arbitrary shapes and structural complexities). Previous research studies show that in some cases LISA outperforms conventional numerical approaches, such as Finite Element (FE) and Finite Difference (FD) methods, in terms of computational accuracy, efficiency and cost, as well as hardware requirements when used to simulate propagating GUWs. In particular when GUWs with short wavelengths and a small time increment in calculation are taken into consideration [43]. Furthermore, LISA introduces a Sharp Interface Model (SIM) to match the particle displacements and stresses at the nodes where the high impedance ratio is present between cells material. In such a way LISA – although being based on the FD discretisation – outperforms the conventional FD algorithms. The advantage of using SIM for modelling wave propagation has been demonstrated in composite laminates [42] and metallic structures [48]. Enhancement in computational accuracy, efficiency and reliability for wave propagation modelling based on LISA with SIM, when compared with the use of then traditional FD methods, has been already confirmed [39,44]. Further work on enhancing the modelling capabilities of the wave propagation within the LISA framework led to the introduction of nonlinear material definitions [49,50]. However, these initial studies have not utilised any systematisation regarding the fundamental development of the LISA iterative equations. Moreover, the linear strain–displacement relation was assumed in those descriptions, where in the current work the Green–Lagrange relation is used. Another direction of developing LISA led to its spin-off known as Spring Model (SM) [51], whereby a faithful depiction of the “breathing” connections between the interfaces of the two adjoining cells can be reached. Therefore, such a feature endows LISA with additional merit to canvass structural damage. Most recently, a new approach for modelling the crack-wave interaction in the LISA environment was presented in [32], where a Coulomb friction model along with the penalty method were integrated to capture the stick-slip contact motions between the crack surfaces.

In the present work, a new nonlinear model of wave propagation based on the LISA and SM framework is presented. A dedicated numerical simulation tool is developed to scrutinise the higher-order harmonic generation and accumulation of nonlinearity along with the wave propagation in fatigued materials bearing a “breathing” crack. Various sources of nonlinearity are considered in two scenarios in which different wave mode pairs (consisting of a fundamental mode and its corresponding second harmonic mode) are considered.

This paper is organized as follows. The theoretical background of the nonlinear hyper-elasticity of elastic medium followed by the description of the new version of LISA used for modelling nonlinear wave propagation are discussed in Section 2. Section 3 outlines the approach used to simulate the “breathing” motion of the fatigue crack. The “breathing” motion is explained based on the higher-order harmonic generation. The SM is introduced to model the “breathing” behaviour of the fatigue crack. Based on LISA and SM, a dedicated approach for modelling the higher-order harmonic generation and accumulation of nonlinearity in GUWs propagating in fatigued materials is developed to interrogate three scenarios. First, the developed modelling approach is validated in Section 4 with the model based on the Finite Element Method (FEM) generated in the commercial software ABAQUS®. Next, in Section 5 the symmetric S0–s0 mode pair at a lower frequency regime, in which case a cumulative growth of the second harmonic magnitude might be observed, and the S1–s2 mode pair at a higher frequency range, which is known and widely used as a “internal resonance” mode pair resulting with the cumulative increase of the second harmonic with the propagation distance, are examined. The upper case letter in the mode pair description corresponds to the first harmonic mode (e.g. S0, S1) and the second harmonic mode is identified with the lower case letter (e.g. s0, s2). Some discussion on the obtained results is also presented in this section. Finally, the conclusions are presented in Section 6.

## 2. Simulation of nonlinearity of GUWs propagating in a nonlinear material

Nonlinearities observed in ultrasonic waves propagating in isotropic and homogeneous solids result from material behaviour (e.g. plasticity, inter-grain contacts, inclusions) and/or structural defects (e.g. elastic effects, viscous-like or thermal losses at fatigue cracks). Two nonlinear effects are important to consider when guided ultrasonic wave propagation is modelled. These are: (i) material hyper-elasticity and (ii) “breathing” motion of structural damage. This section describes the theoretical background of the nonlinear hyper-elastic material definition, which is the base for developing the numerical tool shown in the later part.

### 2.1. Material hyper-elasticity model based on the Landau–Lifshitz’s energy density relation

The nonlinear isotropic hyper-elasticity can be defined using the Landau–Lifshitz’s energy density relation [52]. Denoting the deformation gradient as  $\mathbf{F} = \mathbf{I} + \mathbf{H}$  – where  $\mathbf{I}$  is an identity matrix and  $\mathbf{H} = \mathbf{u} \otimes \nabla$  is the displacement gradient tensor – the Green–Lagrange strain tensor –  $\boldsymbol{\varepsilon}_{\text{GL}}$  – takes the form

$$\boldsymbol{\varepsilon}_{\text{GL}} = \frac{1}{2} (\mathbf{F}^T \mathbf{F} - \mathbf{I}) = \frac{1}{2} (\mathbf{H} + \mathbf{H}^T + \mathbf{H}^T \mathbf{H}), \quad (1)$$

where superscript  $T$  signifies a transposed quantity. The energy density  $U$  is subject to the third-order strain of  $\boldsymbol{\varepsilon}_{\text{GL}}$  [52]:

$$U(\boldsymbol{\varepsilon}_{\text{GL}}) = \frac{\lambda}{2} I_1^2 + \mu I_2 + \frac{1}{3} \mathcal{A} I_3 + \mathcal{B} I_2 I_3 + \frac{1}{3} \mathcal{C} I_1^3, \quad (2)$$

where

$$\begin{aligned} I_1 &= \text{tr}(\boldsymbol{\varepsilon}_{\text{GL}}), \\ I_2 &= \text{tr}(\boldsymbol{\varepsilon}_{\text{GL}}^2), \\ I_3 &= \text{tr}(\boldsymbol{\varepsilon}_{\text{GL}}^3). \end{aligned} \quad (3)$$

$\lambda$  and  $\mu$  are the Lamé constants.  $\mathcal{A}$ ,  $\mathcal{B}$  and  $\mathcal{C}$  are the Landau third-order elastic constants and  $I_1, I_2, I_3$  are the first, second and third isotropic invariants of strain tensor  $\boldsymbol{\varepsilon}_{\text{GL}}$ , respectively ( $\text{tr}(\bullet)$  denotes

the trace of the tensor in the above equation). Through differentiation of the energy density  $U$  with respect to the strain tensor –  $\boldsymbol{\varepsilon}_{\text{GL}}$  – components, one receives the second Piola–Kirchhoff stress tensor ( $T$ ) as [36]

$$T = \frac{\partial U(\boldsymbol{\varepsilon}_{\text{GL}})}{\partial \boldsymbol{\varepsilon}_{\text{GL}}} = \lambda \text{tr}(\boldsymbol{\varepsilon}_{\text{GL}}) + 2\mu \boldsymbol{\varepsilon}_{\text{GL}} + \mathcal{C}(\text{tr}(\boldsymbol{\varepsilon}_{\text{GL}}))^2 \mathbf{I} + \mathcal{B} \text{tr}(\boldsymbol{\varepsilon}_{\text{GL}}^2) \mathbf{I} + 2\mathcal{B} \text{tr}(\boldsymbol{\varepsilon}_{\text{GL}}) \boldsymbol{\varepsilon}_{\text{GL}} + \mathcal{A} \boldsymbol{\varepsilon}_{\text{GL}}^2. \quad (4)$$

For a two-dimensional case, without loss of generality, the stress–strain relation takes the form

$$\begin{aligned} T_{xx} &= (\lambda + 2\mu) \varepsilon_{xx} + \lambda \varepsilon_{yy} + (\mathcal{A} + 3\mathcal{B} + \mathcal{C}) \varepsilon_{xx}^2 \\ &\quad + (\mathcal{B} + \mathcal{C}) \varepsilon_{yy}^2 + (\mathcal{A} + 2\mathcal{B}) \varepsilon_{xy}^2 \\ &\quad + (2\mathcal{B} + 2\mathcal{C}) \varepsilon_{xx} \varepsilon_{yy}, \\ T_{yy} &= (\lambda + 2\mu) \varepsilon_{yy} + \lambda \varepsilon_{xx} + (\mathcal{A} + 3\mathcal{B} + \mathcal{C}) \varepsilon_{yy}^2 \\ &\quad + (\mathcal{B} + \mathcal{C}) \varepsilon_{xx}^2 + (\mathcal{A} + 2\mathcal{B}) \varepsilon_{xy}^2 \\ &\quad + (2\mathcal{B} + 2\mathcal{C}) \varepsilon_{xx} \varepsilon_{yy}, \\ T_{xy} &= 2\mu \varepsilon_{xy} + (\mathcal{A} + 2\mathcal{B}) \varepsilon_{xx} \varepsilon_{xy} + (\mathcal{A} + 2\mathcal{B}) \varepsilon_{yy} \varepsilon_{xy}, \end{aligned} \quad (5)$$

where  $x$  and  $y$  coordinates correspond to the horizontal direction and to the vertical direction, respectively. The  $\varepsilon_{ij}$  with  $i, j = \{x, y\}$  are the components of the  $\boldsymbol{\varepsilon}_{\text{GL}}$ . Subsequently, the Green–Lagrange relation from Eq. (1) can be introduced to the above set of stress–strain relations in order to receive the final stress–displacement dependence, as detailed in Appendix A. The result forms the base for developing the nonlinear iteration equations for LISA and SM models in numerical simulations for wave propagation in nonlinear media.

## 2.2. Modelling wave propagation in hyper-elastic medium using Nonlinear LISA (NL–LISA)

The LISA discretises the analysed structure into a regular grid of rectangular cells. Next, material properties are assumed to be constant within each cell. However these properties may differ between the cells. For the two-dimensional case, each nodal point belongs to four cells. For any particular point – before the equation for the displacement vector is established – the solution is written and treated as continuous within each cell. Then the so-called Sharp Interface Model (SIM) is used to match displacements and stresses – as a result the LISA iteration equations are derived. The SIM leads to more accurate results when wave propagation problems in complex media with large impedance mismatch at interfaces between different materials are investigated. Since the explicit central difference is used for the time domain discretisation, the method is well suited for parallel processing. The parallel algorithm of LISA – implemented on graphical cards – has been proposed and demonstrated in [53].

In order to acquire new iterative equations for the Nonlinear LISA (NL–LISA), the general equation of the wave motion in the nonlinear medium is required. This equation can be obtained by substituting Eq. (1) into (5). After the space derivation of the acquired relations, the simplified form of the wave motion equation in two-dimensional structured can be given as

$$(\lambda + \mu) \mathbf{u}_{,jji} + \mu \mathbf{u}_{,ijj} + f_i^{\text{NL}} = \rho \mathbf{u}_{,itt} \quad i, j = \{x, y\}, \quad (6)$$

where a comma preceding a subscript denotes the differentiation with respect to that subscript variable,  $\rho$  is the material density and  $f_i^{\text{NL}}$  is a forcing term containing the higher-order terms related to the nonlinear material description. Neglecting terms above the second order in displacements allows one to transform Eq. (6) to the matrix notation as

$$\begin{aligned} &AW_{,xx} + BW_{,yy} + CW_{,xy} \\ &+ W_{,x}^F D^x W_{,xx}^{\text{NLF}} + W_{,y}^F D^y W_{,xx}^{\text{NLS}} \\ &+ W_{,x}^F E^x W_{,yy}^{\text{NLF}} + W_{,y}^F E^y W_{,yy}^{\text{NLS}} \\ &+ W_{,x}^F F^x W_{,xy}^{\text{NLS}} + W_{,y}^F F^y W_{,xy}^{\text{NLF}} = \rho \ddot{W}, \end{aligned} \quad (7)$$

where

$$A = \begin{bmatrix} \lambda + 2\mu & 0 \\ 0 & \mu \end{bmatrix}, \quad B = \begin{bmatrix} \mu & 0 \\ 0 & \lambda + 2\mu \end{bmatrix}, \quad C = \begin{bmatrix} 0 & \lambda + \mu \\ \lambda + \mu & 0 \end{bmatrix},$$

are the material matrices corresponding to the linear part of the wave motion equation and

$$D^x = \begin{bmatrix} \lambda + 2\mu + 2\mathcal{A} & 0 & 0 & 0 \\ +6\mathcal{B} + 2\mathcal{C} & & & \\ 0 & \lambda + 2\mu & 0 & 0 \\ 0 & +\frac{\mathcal{A}}{2} + \mathcal{B} & 0 & 0 \\ 0 & 0 & \frac{\mathcal{A}}{2} + \mathcal{B} & 0 \\ 0 & 0 & 0 & \frac{\mathcal{A}}{2} + \mathcal{B} \end{bmatrix},$$

$$D^y = \begin{bmatrix} \frac{\mathcal{A}}{2} + \mathcal{B} & 0 & 0 & 0 \\ 0 & 2\mathcal{B} + 2\mathcal{C} & 0 & 0 \\ 0 & 0 & \mu + \frac{\mathcal{A}}{2} + \mathcal{B} & 0 \\ 0 & 0 & 0 & \mu + \frac{\mathcal{A}}{2} + \mathcal{B} \end{bmatrix},$$

$$E^x = \begin{bmatrix} \mu + \frac{\mathcal{A}}{2} & 0 & 0 & 0 \\ +\mathcal{B} & & & \\ 0 & \mu + \frac{\mathcal{A}}{2} & 0 & 0 \\ & +\mathcal{B} & & \\ 0 & 0 & 2\mathcal{B} + 2\mathcal{C} & 0 \\ 0 & 0 & 0 & \frac{\mathcal{A}}{2} + \mathcal{B} \end{bmatrix},$$

$$E^y = \begin{bmatrix} \frac{\mathcal{A}}{2} + \mathcal{B} & 0 & 0 & 0 \\ 0 & \frac{\mathcal{A}}{2} + \mathcal{B} & 0 & 0 \\ 0 & 0 & \lambda + 2\mu & 0 \\ & & +\frac{\mathcal{A}}{2} + \mathcal{B} & \\ 0 & 0 & 0 & \lambda + 2\mu + 2\mathcal{A} \\ & & & +6\mathcal{B} + 2\mathcal{C} \end{bmatrix},$$

$$F^x = \begin{bmatrix} \frac{\mathcal{A}}{2} + 3\mathcal{B} & 0 & 0 & 0 \\ +\mathcal{C} & & & \\ 0 & \mathcal{A} & 0 & 0 \\ & +2\mathcal{B} & & \\ 0 & 0 & \lambda + \mu + \frac{\mathcal{A}}{2} & 0 \\ & & +3\mathcal{B} + 2\mathcal{C} & \\ 0 & 0 & 0 & \lambda + \mu \\ & & & +\mathcal{A} + 2\mathcal{B} \end{bmatrix},$$

$$F^y = \begin{bmatrix} \lambda + \mu & 0 & 0 & 0 \\ +\mathcal{A} + 2\mathcal{B} & & & \\ 0 & \lambda + \mu + \frac{\mathcal{A}}{2} & 0 & 0 \\ & +3\mathcal{B} + 2\mathcal{C} & & \\ 0 & 0 & \mathcal{A} & 0 \\ & & +2\mathcal{B} & \\ 0 & 0 & 0 & \frac{\mathcal{A}}{2} + 3\mathcal{B} \\ & & & +\mathcal{C} \end{bmatrix},$$

are the material matrices corresponding to the nonlinear part of the wave motion equation. Finally,

$$W = \begin{bmatrix} u \\ v \end{bmatrix}, \quad W^F = \begin{bmatrix} u & v & 0 & 0 \\ 0 & 0 & u & v \end{bmatrix},$$

$$W^{NLF} = \begin{bmatrix} u \\ v \\ v \\ u \end{bmatrix}, \quad W^{NLS} = \begin{bmatrix} v \\ u \\ u \\ v \end{bmatrix}, \quad (8)$$

are the displacement vectors/matrices forms required for the matrix notation of the wave motion equation.

From this point the procedure to receive the final iteration equations follows the one with linear material definition, which is available in [39,53] and is omitted in this work due to its long form. Details of the further steps are available in [54]. Hence, this section covers modelling of the second harmonic generated due to the nonlinearity of the material.

### 3. Simulating higher-order harmonic generation induced by a “Breathing crack

Another source of nonlinearity in guided wave propagation considered in this paper is the “breathing” crack phenomenon, which can be exhibited by contacting faces of fatigue cracks. This section presents how the SM can be used in the NL–LISA framework to model the nonlinear “breathing” crack phenomenon.

#### 3.1. “Breathing” crack

The “breathing” crack is a well-known phenomenon in nonlinear dynamics. The simplest model of this phenomenon involves a bi-linear spring that introduces different elastic moduli for the open and closed crack. More accurate physical models often involve the contact of crack faces, friction, crack tip plasticity and even temperature gradients near crack tips, as described in [55]. In nonlinear acoustics – when ultrasonic waves are used for damage detection – this nonlinear behaviour is known under the name “clapping” or Contact Acoustic Nonlinearity (CAN) [25]. CAN involves the interaction between propagating ultrasonic waves and imperfect interfaces of fatigue cracks. As a result higher-order harmonics are generated. A graphical illustration of the nonlinear “breathing” crack phenomenon is demonstrated in Fig. 1. The crack closes when the compressional part of the propagating wave reaches its interface. When the crack faces are in contact (i.e. the crack is closed), the undisturbed ultrasonic wave penetrates through the crack. The tensile part of the propagating wave causes the opening of the crack, leading to the partial wave reflection.

#### 3.2. Modelling of “Breathing” crack using Spring Model (SM)

The SM is used in order to model the “breathing” crack phenomenon. Wave propagation in this model is substituted by the movement of the equivalent set of excited “tensorial” springs.

The discretisation scheme and material definition in the SM follow those of LISA. The major difference between the two approaches is found in the nodal displacement analysis. In a two-dimensional case in LISA, each nodal point belongs to four cells. On the other hand, in SM each nodal point is divided into four sub-nodal points, each of which belongs to a cell. As a result, the relations between the sub-nodes are defined via “tensorial” springs and used for force representation. Forces between the sub-nodes within one cell are named external forces  $F$  and forces between the cells, introduced in order to keep the continuity of the structure, are named internal forces  $f$ . A graphical representation of discretisation schemes for both methods is shown in Fig. 2.

Although the iteration procedure in the SM method differs from the one of the LISA method, the same final result can be achieved for both approaches, assuming that there is a perfect contact between the cells of the structure. The final result will have a form

$$w_{t+1} = 2w - w_{t-1} + \frac{(\Delta t)^2}{\rho \varepsilon^2} \sum_{k=1}^4 \bar{F}^k, \quad (9)$$

where  $w_{t+1}, w, w_{t-1}$  are the respective iteratives of displacement in time,  $\Delta t$  is the time discretisation step,  $\rho$  is the sum of the densities of the cells around the node for which the displacement values are calculated,  $\varepsilon$  is the size of the element,  $\sum_{k=1}^4 \bar{F}^k$  is the sum of the resultant forces from the four cells ( $k$  indicates the cell number) surrounding the analysed node. Eq. (9) corresponds to the arrangement shown in Fig. 2a and the displacements are calculated for node  $P$  in each time step.

Imperfect contact between the cell’s interfaces can be introduced by the division of node  $P$  from Fig. 2a into four sub-nodes  $P_{1-4}$ , as illustrated in Fig. 2b. This approach redefines the final iteration equations. Four independent equations for each sub-node can be written in the form

$$w_{t+1}^{(k)} = 2w^{(k)} - w_{t-1}^{(k)} + \frac{(\Delta t)^2}{\rho \varepsilon^2} \left( \bar{F}^k + \sum_{l \neq k} \bar{f}_{kl}^{(pc)} \right), \quad (10)$$

$(k, l = 1, \dots, 4),$

where in order to maintain the continuity of the structure, the internal forces  $\bar{f}_{kl}^{(pc)}$  for perfect contact are introduced in the form

$$\bar{f}_{kl}^{(pc)} = \frac{\rho_k \bar{F}_l - \rho_l \bar{F}_k}{\rho}, \quad (11)$$

where  $\rho_k$  and  $\rho_l$  are the densities of the cells between which the internal force is determined. Here,  $\bar{F}_k$  and  $\bar{F}_l$  are the respective external forces of each cell. This component allows one to extend the model, so imperfect contact between the interfaces can be used. This can be achieved by introduction of the contact quality factor  $Q_{kl}$  for each sub-node through the relationship

$$\bar{f}_{kl} = Q_{kl} \bar{f}_{kl}^{(pc)}. \quad (12)$$

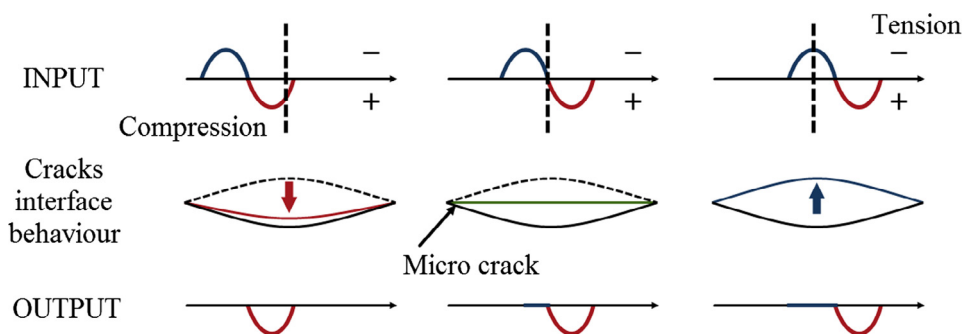


Fig. 1. Schematic diagram of a “breathing” crack (the compressional part of the propagating wave is penetrating the fracture, while the tensile is not). Adopted from [25].

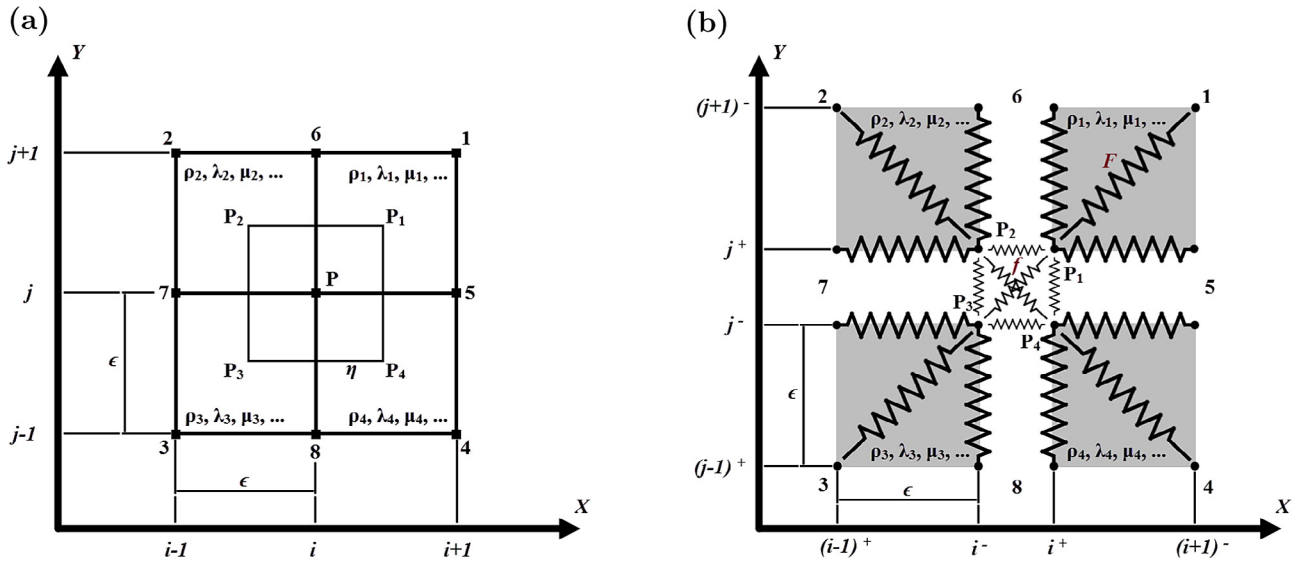


Fig. 2. Discretisation of the wave propagation model using: (a) LISA (adopted from [39]); and (b) SM (adopted from [51]).

The  $Q_{kl}$  factor may vary between 0 and 1, giving the possibility of modelling different types of imperfections in the analysed structure. The contact quality factor may differ from one sub-node to the other sub-node and – what is more important – different values can be defined for the  $x$  and  $y$  components of the internal forces.

In this work, the changing state of the factor  $Q_{kl}$  is used to model the “breathing” crack phenomenon. The normal stress at the  $x$ -direction between the cracks faces is calculated at every simulation time step and is used to determine of whether the gap between the crack interfaces is opened or closed. Mathematically this can be described using the following relation

$$\begin{aligned} \sigma_{xx} \leq 0 \quad Q_{kl} &= 1, \\ \sigma_{xx} > 0 \quad Q_{kl} &= 0. \end{aligned} \tag{13}$$

When the compressional part of the propagating stress wave reaches the crack surfaces, the perfect contact is imposed by setting  $Q_{kl}$  as 1; whereas for the tensile part of the wave it is set to 0. Thus, through such action higher-order harmonics are imposed on the propagating ultrasonic wave responses. Fig. 3 gives an example illustrating the presence of the “breathing” crack in ultrasonic response. Here, the displacement signals from the undamaged and damaged (i.e. cracked) structures are compared in both, i.e. time and frequency, domains.

One can easily notice that the amplitude of the time domain signal in Fig. 3a for the damaged case is cut-off. This is equivalent to the open state ( $Q_{kl}$  being equal to 0) of the “breathing” crack. Below that level the wave is undisturbed which suggests that at the specific period of time the crack is closed ( $Q_{kl}$  being equal to 1). The “breathing” crack action has also an effect on the frequency representation, where higher-order harmonics are generated, as shown in Fig. 3b.

It is important to note again that the contact quality factor  $Q_{kl}$  may vary between the nodes. Thus the condition of opening and closing the crack is considered separately and independently for each node. As a result, more complex interactions between crack faces can be modelled when numerical simulations of wave propagation are performed.

#### 4. Validation with Finite Element Method (FEM)

First, the commercial software ABAQUS® – based on FEM – was used to validate numerically the proposed NL-LISA/SM platform for nonlinear wave propagation and wave interaction with damage. Two model definitions were interrogated, i.e. (i) when the nonlinear material definition was the only source of the higher-order harmonics generations; and (ii) when two sources of nonlinearity were present, namely the nonlinear material and the “breathing” crack.

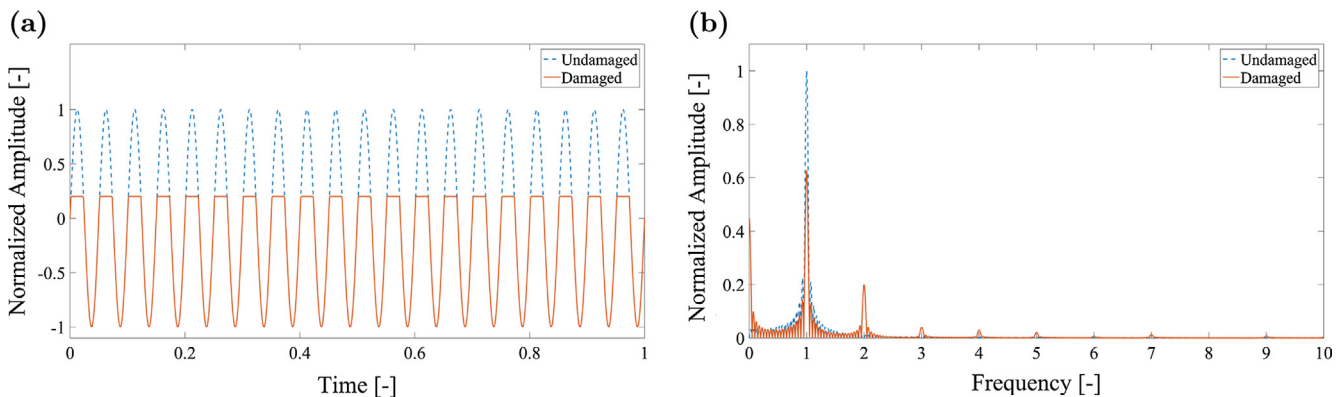


Fig. 3. Ultrasonic response from structures with and without the “breathing” crack. The signals are presented in: (a) time domain; (b) frequency domain.

The nonlinear material was modelled within the ABAQUS® with the application of the VUMAT subroutine [11]. Aluminium was chosen as the material in this analysis with the properties as summarised in Table 1.

The thickness of the beam was set as 2 mm and the length was equal to 1400 mm. Two structures were modelled, i.e. the undamaged beam and the beam damaged with a “breathing” crack. The crack was introduced 300 mm from the left hand side of the beam (as marked by the black vertical line in Fig. 4). The depth of the crack was set to 50% of the beam thickness. The in-plane displacement excitation was used, which was placed on the left hand side of the beam and was uniformly distributed along the thickness of the beam (as marked with green arrows in Fig. 4). This arrangement allowed for selective excitation of the symmetric Lamb wave mode.

The five-cycled sine burst signal – enveloped by the Hanning window – was used as the excitation signal. The excitation frequency was equal to 100 kHz. The amplitude of the excitation signal was set as 1 μm. Due to such choice of the amplitude, only small but finite strains conditions are ensured to avoid plastic deformation. The thickness of the beam and the selected excitation frequency lead in theory to two Lamb wave modes propagating in the analysed structure, as demonstrated in Fig. 5. However, in practice the selected excitation approach allows only for single S0 Lamb wave mode propagation; the amplitude of the second mode is negligible. Lamb wave in-plane displacement responses were collected at the distance of 850 mm from the left hand side of the beam (marked with the red pointer in Fig. 4). The time discretisation was set to 5 ns and the space was discretised with the 0.1 mm square elements.

Fig. 6 presents simulated Lamb wave responses in the time and frequency domain collected from the models with only nonlinear material definition. A very good agreement between the NL-LISA- and FEM-based numerical simulations can be observed. In the time domain responses in Fig. 6a are almost perfectly matched and no major difference can be observed between the results from two different methods. The frequency domain results in Fig. 6b also display similar results for both methods investigated. Some minor differences can be observed above 600 kHz. However, these differences are outside the frequency range of interest covering the first and second harmonics.

Similar numerical simulations were performed again, however this time the “breathing” crack model was additionally introduced to the beam. Fig. 7 shows the collected and processed results in both, time and frequency, domains. It can be noticed that the time domain signals from two methods agree with each other with very slight differences. That small difference is caused by the DC component exhibited in the frequency spectrum in Fig. 7b (around 0 Hz), which for the model in ABAQUS® is slightly higher than in the model from NL-LISA/SM. Nevertheless, the relevant magnitudes for the fundamental component and the second harmonic match reasonably well. Higher-order harmonics exhibit larger differences when the results from both simulation methods are compared.

To sum up, the initial nonlinear Lamb wave propagation results from the proposed NL-LISA/SM-based numerical simulation platform produce very good results in the time and frequency domains when compared with the commercial FEM software. Arrival times in the time domain and amplitudes of the first two harmonics in

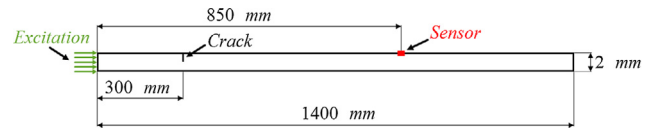


Fig. 4. Two-dimensional 2 mm thick beam model used for nonlinear Lamb wave propagation modelling based on the proposed NL-LISA/SM platform and with FEMs.

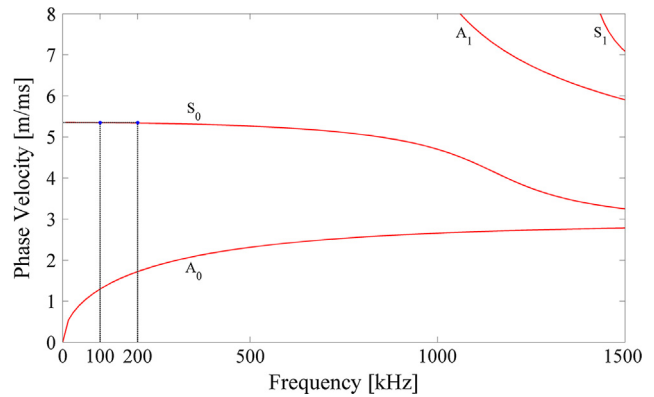


Fig. 5. Lamb wave dispersion curves for the 2 mm thick aluminium beam used in numerical simulations.

the frequency domain do not exhibit significant differences when the nonlinear model of material and crack are introduced to the beam. The following section investigates the effect of material nonlinearity, damage severity, wave propagation distance and excitation frequency on higher-order harmonic generations.

### 5. Proof-of-concept

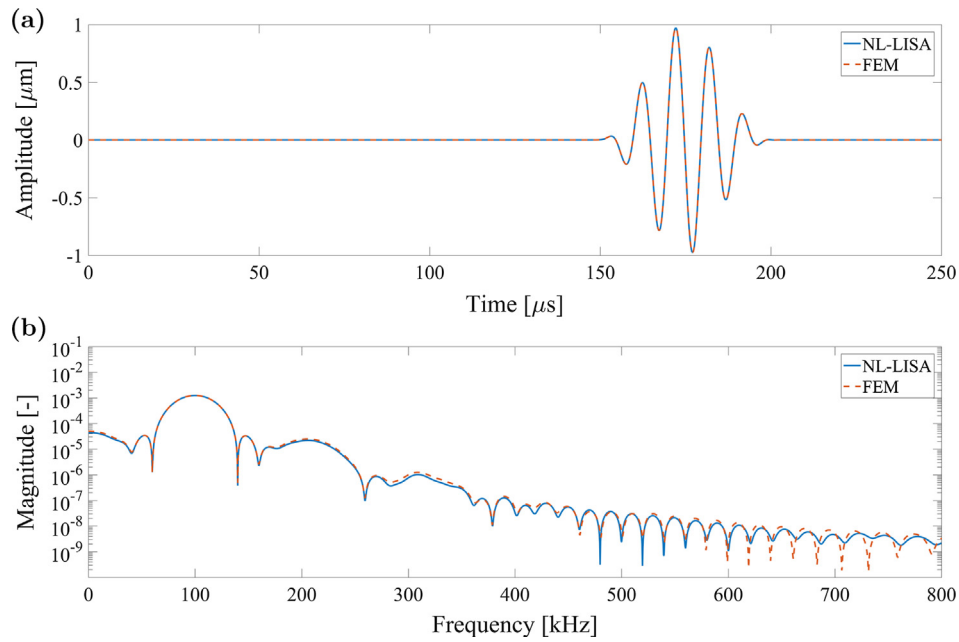
This section demonstrates how the nonlinear material and “breathing” crack model – described respectively in Sections 2.2 and 3.2 – influence the wave propagation in different scenarios.

It is important to note that when higher-order harmonic generation is used for damage detection in Lamb wave propagation, the experimental set-up (excitation frequencies in particular) should be selected to enhance amplitude of higher harmonics due to damage and to suppress this nonlinear effect due to material inheritance. However, in this work due to the chosen frequencies, an extreme approach is taken into consideration, namely, where both “breathing” crack and the nonlinear material have a significant impact on the generated second harmonic. Such a choice of investigation gives an opportunity to clarify whether or not it is possible to identify the presence and the stage of the fatigue “breathing” crack in the structure with highly nonlinear material properties. The results of this investigation can be used to obtain the knowledge required to develop the new approach of the damage detection and identification in the fields of NDE and SHM. Therefore, due to the successful validation of the developed NL-LISA/SM modelling method, two following scenarios are investigated.

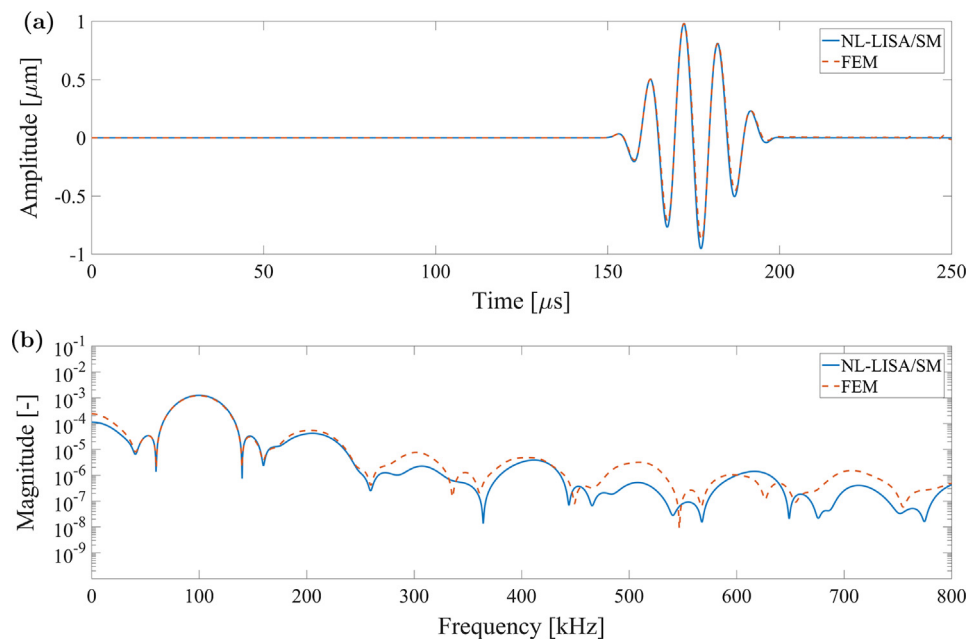
In the first scenario, the low frequency region in the Lamb wave frequency–wavenumber space is investigated. The focus in these investigations is on the symmetric S0-s0 (where S0 is the

Table 1  
Material properties of aluminium used in nonlinear wave propagation.

Young's modulus	Poisson's ratio	Density	Landau's Third-Order Elastic Constants [56]		
$E$	$\nu$	$\rho$	$\mathcal{A}$	$\mathcal{B}$	$\mathcal{C}$
68.9 GPa	0.33	2700 kg/m <sup>3</sup>	–320 GPa	–200 GPa	–190 GPa



**Fig. 6.** Nonlinear Lamb wave responses: (a) time domain; (b) frequency domain (logarithmic scale). Numerical simulations were performed for the undamaged beam and nonlinear material model, using the NL-LISA platform and FEM.



**Fig. 7.** Results from the models prepared using NL-LISA/SM and FEM with nonlinear material definition and “breathing” crack compared in: (a) time domain; (b) frequency domain (logarithmic scale). The signals are collected at the distance of 850 mm.

fundamental mode and the  $s_0$  is its second harmonic mode) Lamb wave mode pair. This mode pair is chosen due to the fact that in the considered frequency band only two Lamb wave modes are possible to propagate. Moreover, the fundamental symmetric mode has almost non-dispersive characteristic. This desired property has already come to the attention of some previous investigations on nonlinear Lamb waves [14,57]. In addition, both the fundamental  $S_0$  mode and its  $s_0$  harmonic have approximately the same phase and group velocities. The phase velocity matching is particularly important, since it is generally accepted that the cumulative amplitude increase of the propagating second harmonic requires perfect matching of phase velocities and the non-

zero power flux between the considered Lamb wave modes. Therefore, the wave propagation characteristics are investigated to find out whether the  $S_0$ - $s_0$  mode pair can also be considered as a cumulative synchronous mode pair. The same group velocity of both harmonics simplifies the analysis of the considered wave mode packages.

In the second scenario investigated, the wave propagation characteristics of the well-known synchronised  $S_1$ - $s_2$  (i.e. the fundamental symmetric  $S_1$  mode and the second harmonic symmetric  $s_2$  mode) pair in the high frequency region of the Lamb wave frequency-wavenumber space is considered. The  $S_1$ - $s_2$  mode pair is of great interest to the ultrasonic community [26,27,29] when the

cumulative effect of the generated second harmonic is investigated for damage detection. Both numerical simulation scenarios aim to investigate the effect of material nonlinearity, severity of damage and wave propagation distance on damage detection.

### 5.1. S0–s0 Lamb wave mode pair

Firstly, the nonlinear behaviour of the S0–s0 Lamb wave mode pair was simulated for the undamaged and damaged beam. A two-dimensional model presented in Section 4 with material properties from Table 1 was used in this section as well. Seven depths of the fatigue crack were investigated as the percentage of the beam thickness (from 0 to 60% every 10%). The excitation signal and frequency was the same as described in Section 4. However, this time a point-like excitation (indicated as a green arrow in the top-left corner of the beam in Fig. 8) with the assigned in-plane displacement was used in order to narrow the influence of the excitation type on wave propagation characteristics. Finally, the sensing space was chosen on the upper surface of the beam and the in-plane displacement response was gathered every 50 mm starting from the left hand side of the beam until 1200 mm. The sensing area was intentionally smaller than the actual length of the beam in order to avoid mixed direct incident and reflected (from the edge of the beam) wave propagation components. Square elements were used with the size equal to 0.1 mm and the simulation time step was set as 5 ns to maintain the numerical stability of the model. The schematic diagram of the beam model is shown in Fig. 8.

Figs. 9a and b present numerical simulation results for the linear and nonlinear material models, respectively. In both cases Lamb wave response are presented in the time and frequency domains. The results show that since the point-like excitation was used, both Lamb wave modes – i.e. symmetric S0 and antisymmetric A0 – were excited in the analysed structure. Furthermore, due to the interaction of both modes with the fatigue “breathing” crack, converted modes are generated and can be seen after the first S0 wave mode package. At the end of the time responses the fundamental A0 mode interacts with the reflected S0 mode. A rectangular window – displayed in the upper parts of Figs. 9a and b – indicates the extracted S0 mode that was used to obtain the frequency spectra given in the lower parts of these figures. The results in the time and frequency domains are given for different damage severities.

From the frequency representation of the first arrived S0 Lamb wave mode packages extracted from the time signals one can observe that the amplitude of the generated second harmonic increases along with the crack depth. This observation can be made for both cases investigated, i.e. linear and nonlinear material model. Moreover, the magnitudes of the remaining higher-order harmonics increase with the size of the crack as well. However, please note that although these values of magnitudes may seem close to the values of the second harmonic, they are in fact smaller by an order. The misconception may be caused by the fact that the results in the frequency domain are presented in the logarithmic scale. As an example, the results from the beam with nonlinear material definition and for the damage size being equal to 60% of the beam thickness are presented: 1st harmonic  $4.972e-4$ ; 2nd

harmonic  $1.582e-5$ ; 3rd harmonic  $8.378e-7$ ; 4th harmonic  $2.297e-6$ ; 5th harmonic  $4.055e-7$ ; 6th harmonic  $8.208e-7$ , etc. Finally, an increase with the crack size can be also observed in the case of the DC component (around 0 Hz). This effect results from the internal resonance between the DC component, first and second harmonic, as previously shown in [58]. Further investigations are omitted as the characteristics of the DC component are not in the scope of this paper.

The magnitudes of the first and second harmonics were estimated from the frequency spectra. Exact points where the magnitudes were gathered are indicated by the black vertical lines in Fig. 9. The relative acoustic nonlinear parameter  $\beta'$  was calculated as the ratio of the second harmonic magnitude to the square value of the first harmonic magnitude ( $\beta' = A_2/A_1^2$ , where  $A_2$  is the second harmonic magnitude and  $A_1$  is the first harmonic magnitude). This parameter is often utilised for the assessment of damage severity when second-order harmonic generation is used for damage detection [11,31]. The first-, second-order harmonic and  $\beta'$  magnitudes were estimated for different wave propagation distances and damage severities. The results are given in Figs. 10 and 11 for the linear and nonlinear material models, respectively.

The analysis of results in Figs. 10 and 11 clearly shows that the major difference in propagation characteristics are due to the definition of the material. The results given in Figs. 10a and 11a demonstrate that the magnitude of the fundamental harmonic decreases with the severity of damage for the linear and nonlinear material. In contrast, the magnitude of the nonlinear parameters investigated increases with the severity of damage. Also, in both cases investigated (i.e. linear and nonlinear material) the magnitude of the fundamental Lamb wave S0 mode does not change significantly in Figs. 10a and 11a with the propagation distance. Similarly, the second harmonic of the S0 Lamb wave mode (i.e. the s0 mode) – generated by the crack – exhibits in Fig. 10b nearly constant magnitude when the linear material model is used in numerical simulations. As a consequence the relevant  $\beta'$  parameter in Fig. 10c also does not change with the wave propagation distance. The reason behind such behaviour lies in the local characteristic of the analysed source of nonlinearity in the structure, i.e. the “breathing” crack. When the fundamental wave mode approaches the crack interfaces, the second harmonic mode is generated from the crack–wave interaction. This second harmonic mode continues to propagate undisturbed as there are no additional nonlinear events in the structure which could force the energy transfer from the primary wave mode to the secondary wave mode.

In contrast, when the nonlinear material model is used in numerical simulations, the magnitude of the second harmonic s0 mode and the relevant  $\beta'$  parameter increase linearly with the wave propagation distance in Figs. 11b and c, respectively. It is important to note that this behaviour can be observed also for the undamaged beam. Such phenomenon is caused by the defined global nonlinearity (nonlinear material model) which forces continuous energy transfer between the fundamental and second harmonic modes through the whole propagation distance. This observation confirms that the S0–s0 mode pair can be treated as the approximate synchronous one for the certain range of frequencies, i.e. the almost non-dispersive frequency region with only two Lamb wave (S0 and A0) modes being excitable. Furthermore, as the fundamental wave approaches the “breathing” crack, after the crack–wave interaction, another (or additional) second harmonic is generated causing the increase of the resulting magnitude of the second harmonic. This magnitude jumps up more for larger damage severities and then continues to grow with the propagation distance.

Due to the presence of the approximate phase velocity matching it is possible to observe a beat-period of the second harmonic

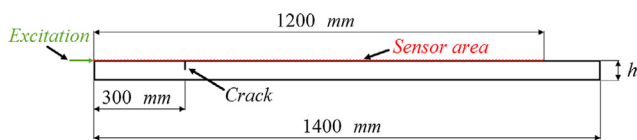
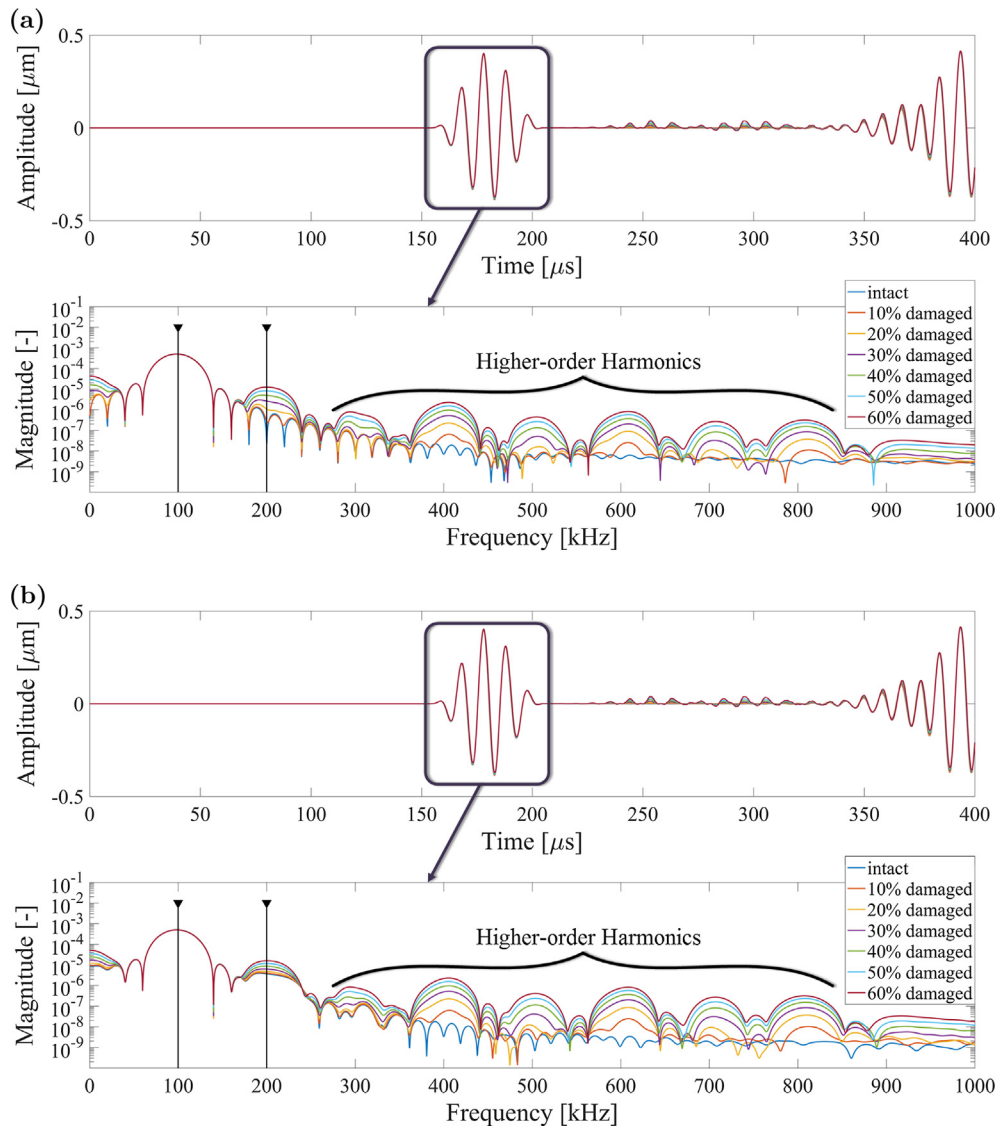


Fig. 8. Two-dimensional  $h = 2$  mm thick beam model used for the nonlinear crack–wave interaction modelling based on the proposed NL–LISA/SM platform. The S0–s0 Lamb wave mode pair is considered in these investigations.



**Fig. 9.** Simulated time- and frequency-domain (logarithmic scale) Lamb wave responses collected at the distance of 850 mm from the excitation site. Numerical simulation were performed for seven different damage severities. The work involved: (a) linear material model; (b) nonlinear material model.

magnitude within the domain of the propagation distance as exhibited in [59]. In the mentioned article, the beat-period appears around 4500 mm from the excitation site, which can be considered as a very long distance for the propagating Lamb waves. With respect to the case presented in this paper, the model required to illustrate the beat-period would be much longer than the one presented by Wan et al. It is therefore questionable to perform such analysis considering both the physical (attenuation and amplitude changes along the propagation path, hardly possible experimental validation) and numerical aspects (error accumulation due to time integration and numerical spectral properties). Instead, a curve fitting procedure was performed on the available data of the second harmonic magnitude pattern in the domain of propagation distance. The data points were acquired from the intact model with nonlinear material (Fig. 11b marked as “intact”). Subsequently, parametrized sine function was used as a base to extrapolate the numerical data in order to receive the values of second harmonic magnitude at longer distances from the source. For the process of curve fitting, the MATLAB Curve Fitting application was used. A sine function was used for extrapolation as  $y = a_1 * \sin(b_1 * x + c_1)$ , where  $x$  is the propagation distance and

$y$  is the magnitude of the second harmonic. Parameters  $a_1 = 2.046e - 05$ ,  $b_1 = 0.0002085$  and  $c_1 = 0.005705$  were generated with the MATLAB Curve Fitting application. The results are presented in Fig. 12. The full circles in the presented plot are the values from numerical model and the solid line depicts the extrapolated response. One can observe that the approximate linearity of the second harmonic growth can be assumed for distances below 4000 mm from the source of excitation.

From the presented curve fitting procedure, the length of the beat-period will have approximately 15600 mm. On the other hand, an analytical way to investigate the beat-period is available by calculating the dispersion length – as shown in [27] – with the form  $L_n = 1 / |k^* - 2k|$ . The  $k^*$  is the wavenumber of the second harmonic mode and  $k$  is the wavenumber of the first harmonic mode. From the above equation the length of the beat-period for the chosen S0–s0 mode pair is approximately 16580 mm, which gives a good agreement with the numerical value obtained from the curve fitting.

Further analyses of the results presented in Figs. 10 and 11 demonstrate that for the S0–s0 Lamb wave mode pair the (in-phase) positive interaction between the second harmonic s0 mode

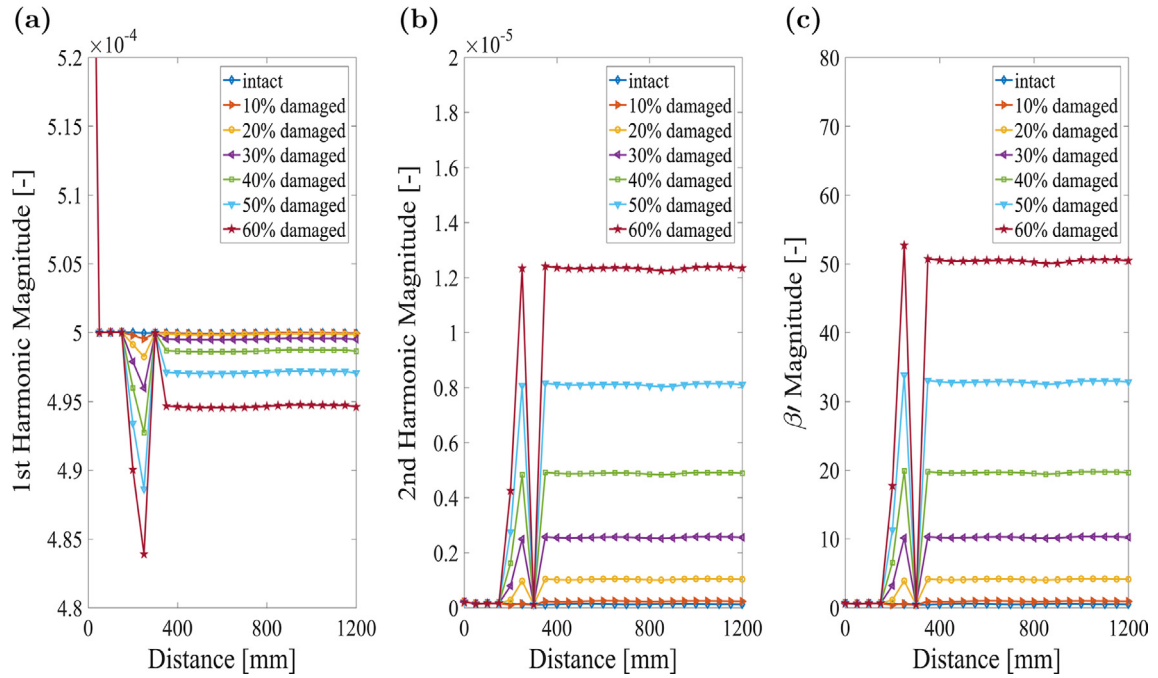


**Fig. 10.** Nonlinear parameters from undamaged and damaged beam models in the propagation distance domain: (a) First harmonic magnitude; (b) Second harmonic magnitude; (c)  $\beta_r$  magnitude. The results were obtained for the S0–S0 mode pair and linear material model.

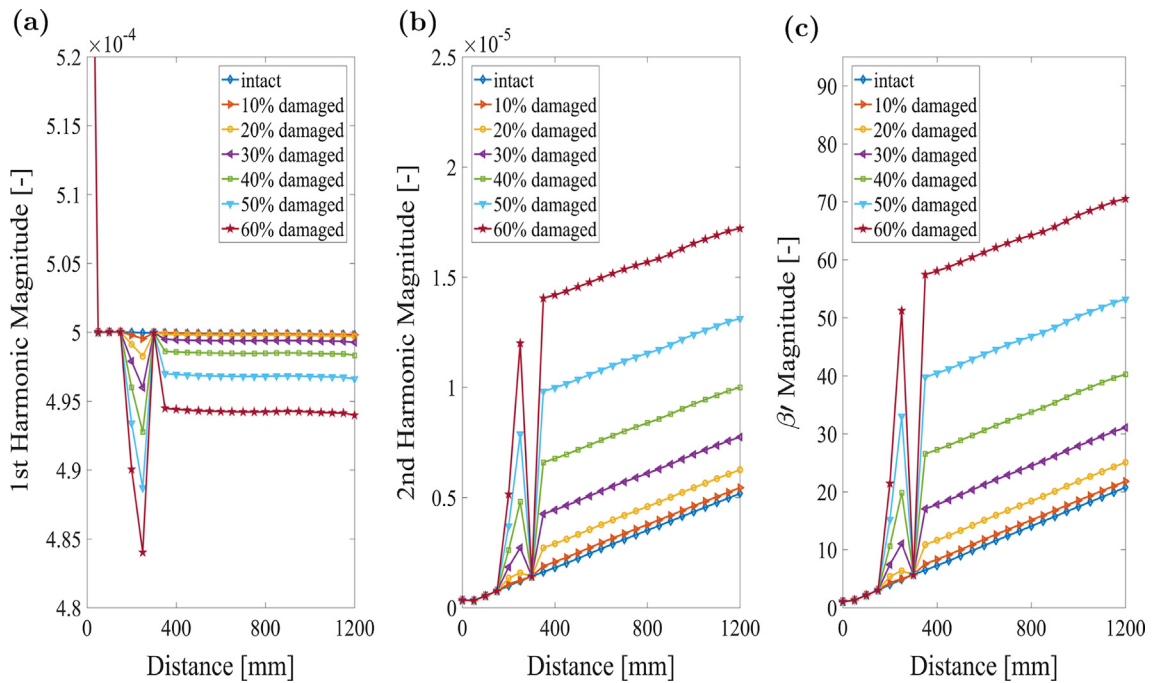


**Fig. 11.** Nonlinear parameters from undamaged and damaged beam models in the propagation distance domain: (a) First harmonic magnitude; (b) Second harmonic magnitude; (c)  $\beta_r$  magnitude. The results were obtained for the S0–S0 mode pair and nonlinear material model.

generated from the local nonlinearity (“breathing” crack) and the second harmonic S0 mode generated from the global nonlinearity (nonlinear material model) takes place, resulting in increased magnitudes. A better insight into the above described phenomena can be obtained when the results for the linear and nonlinear material models and simulated for the intact (i.e. undamaged) and 60% cracked–beam are given in Fig. 13.

The results presented in Fig. 13b confirm the earlier stated explanation regarding the in-phase magnitude summation of the second harmonic S0 modes generated from two different sources

of nonlinearities. It can be clearly seen that the results for the damaged case in the model with nonlinear material definition (dashed red line with the description of “60% damaged – nonlinear mat”) is a sum of the intact nonlinear model (dashed blue line with the description of “intact – nonlinear mat”) and the damaged case with the linear material definition (solid red line with the description of “60% damaged – linear mat”).

When the results for the two different material models are compared (Fig. 13a) the influence of the global material nonlinearity can be observed. The first harmonic magnitudes – resulting from

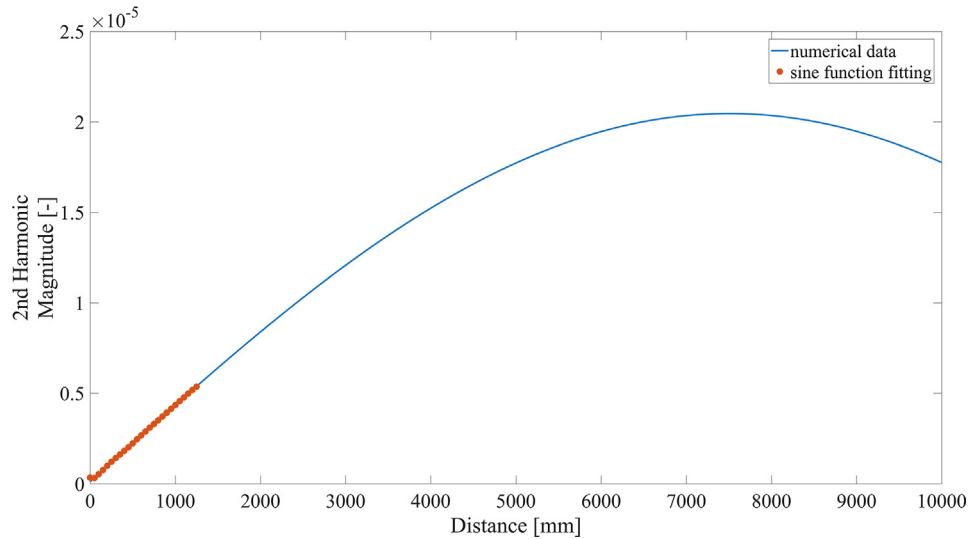


**Fig. 12.** The beat-period of the second harmonic magnitude obtained through the curve fitting process to the numerical data. The data is from the intact model with nonlinear material definition and propagating S0-s0 mode pair.

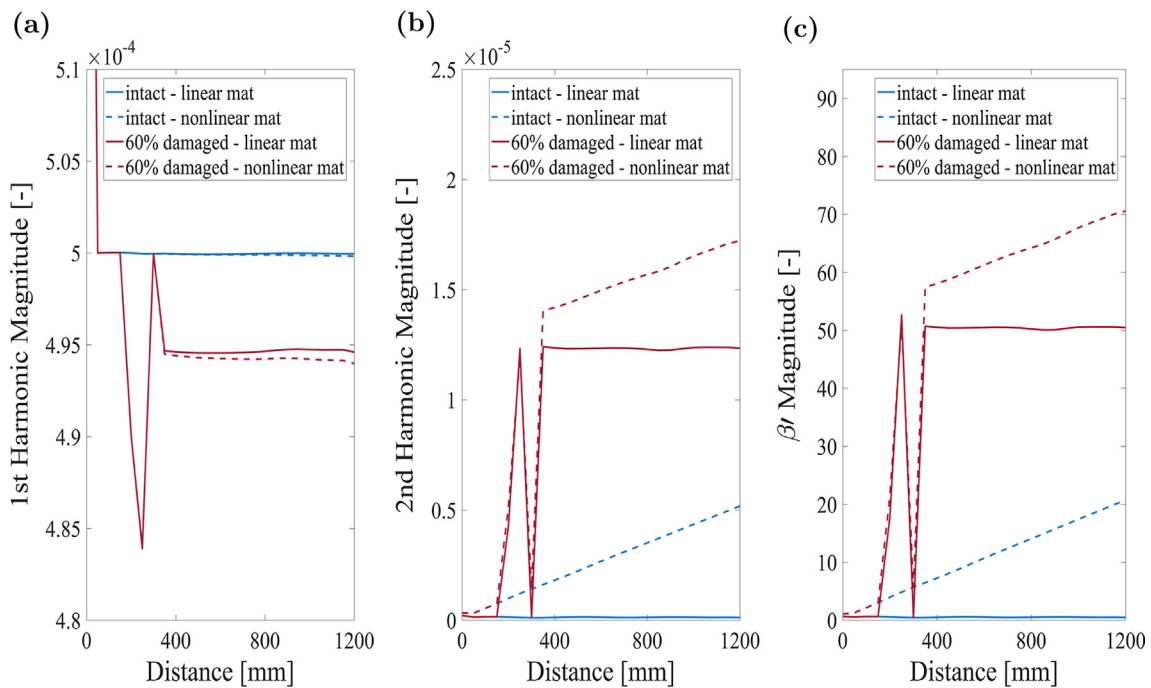


**Fig. 13.** Dependence of the nonlinear parameters on the propagation distance (S0-s0 mode pair), collected from both – i.e. linear and nonlinear – material models: (a) First harmonic magnitude; (b) Second harmonic magnitude; (c)  $\beta'$  magnitude. The results are given only for the intact (undamaged) beam and 60% cracked-beam.

the nonlinear material model – are lower than the relevant magnitudes for the linear material model. This behaviour is caused by the unceasing energy shift from the first to the second harmonic, as already mentioned above. Finally, the nonlinear  $\beta'$  parameter shown in Figs. 10c, 11c and 13c exhibits similar pattern to the second harmonic magnitude. This is due to the fact that the changes of the first harmonic magnitude are not significant with the propagation distance.

Some comments are needed regarding the characteristics of all analysed parameters in the area before the “breathing” crack (distance from 0 to 300 mm). For the second harmonic and  $\beta'$  parameter magnitudes an increasing peak can be observed whereas for the first harmonic a drop of the magnitude is maintained in the

vicinity of the crack. These features result from mixing of incident and crack-reflected wave packages, as observed and described in [46,47]. Furthermore, it is mentioned in [47] that within the close area of the damage a significant increase of the first harmonic magnitude should be observed. No such phenomena is visible in the results presented in this article. It is due to the chosen step between the sensing points (50 mm) which is large enough to make impossible to observe such a characteristic.

Finally, the dependence of the analysed parameters on the size of the crack is scrutinised. In order to achieve this, the simulated results are collected from the point at the distance of 850 mm from the left hand side of the beam and are presented in the crack size domain in Fig. 14.

An exponential growth of the second harmonic magnitude and the relative acoustic nonlinear parameter  $\beta'$  with damage severity can be observed for both – i.e. linear and nonlinear – material models (Figs. 14b and c). The second harmonic generated by the global hyper-elastic nonlinear material model is higher than generated by the local nonlinear crack, as discussed above. The results also show that as the damage severity increases, the magnitude of the second harmonic (and consequently the magnitude of the  $\beta'$  parameter) get closer for the linear and nonlinear material models. With the growth of the crack depth, the influence of the material nonlinear characteristic on the generated second harmonic becomes less significant. The S0–s0 mode pair is more suitable for detection of larger cracks (crack depth larger than 20% of the beam thickness). It is easier to differentiate their influence on the generated second harmonic than the near-surface cracks (up to 20% of the beam thickness). Last but not least, the magnitude of the fundamental harmonic decreases nonlinearly with the damage severity, as expected. The material model does not have a significant effect on this characteristics.

## 5.2. S1–s2 Lamb wave mode pair

This section reports the results obtained from numerical simulations of another synchronous Lamb wave mode pair, i.e. the higher-order symmetric S1–s2 mode pair. This mode pair offers good synchronisation, guarantees cumulative amplitude over propagation distance of the second harmonic and therefore has been widely explored for nonlinear Lamb wave propagation [11,27,28,60].

Again, a two-dimensional aluminium beam with material properties given in Table 1 was used to examine wave propagation and wave interaction with damage of the S1–s2 mode pair. This time the thickness  $h$  of the beam was increased to 4 mm in order to maintain good numerical stability of the selected modes and most importantly in order to reduce the influence of numerical dispersion common to higher-order Lamb wave modes, as demonstrated in [49,58]. Fig. 8 gives the geometry of the beam together with

damage and sensors placing. As in the previous modelling scenario, in-plane displacement responses were collected on the distance of 1200 mm from the left hand side of the beam every 50 mm (marked with red dots in Fig. 8). The selected distance and length of the beam guarantee long propagation and avoids undesired interactions of the incident wave with the edge-reflected components. Furthermore, seven damage severity cases were prepared with the size of the crack increasing from 0% to 60% of the beam thickness (step between the sizes was set to 10%). The crack was positioned 300 mm from the left side of the beam. The excitation was imposed on the top-left corner of the beam a in-plane displacement with the amplitude as in the previous sections. The discretisation in the time and space domain was the same as in the numerical simulations reported in Sections 4 and 5.1.

The excitation frequency was selected following previous research studies [26,29] in order to meet the synchronism condition. For the aluminium beam with material parameters stated in Table 1 the synchronism condition occur at 3.57 MHz \* mm for the S1 fundamental mode and 7.14 MHz \* mm for the second harmonic s2 mode, resulting in the frequencies of 892.5 kHz and 1.785 MHz, respectively for the 4 mm thick beam. Both frequencies of interest are marked on the dispersion curves presented in Fig. 15 to illustrate the synchronisation condition. One can clearly see that both chosen frequencies correspond respectively to the S1 and s2 symmetric modes and the phase velocity matching condition is also satisfied.

A twenty-cycle sine wave burst signal – enveloped by the Hanning window – was used as the excitation. The excitation frequency was equal to 892.5 kHz. Two (linear and nonlinear) material models and seven damage severities were investigated, as explained in Section 5.1.

The dispersion characteristics given in Fig. 15 shows that four Lamb wave modes will be excited in the beam for the selected excitation frequency. In addition, converted modes will be also excited in the beam as a result of the crack–wave interaction, as explained in the previous section. Thus the classical spectral analysis – used in Sections 4 and 5.1 to obtain frequency domain

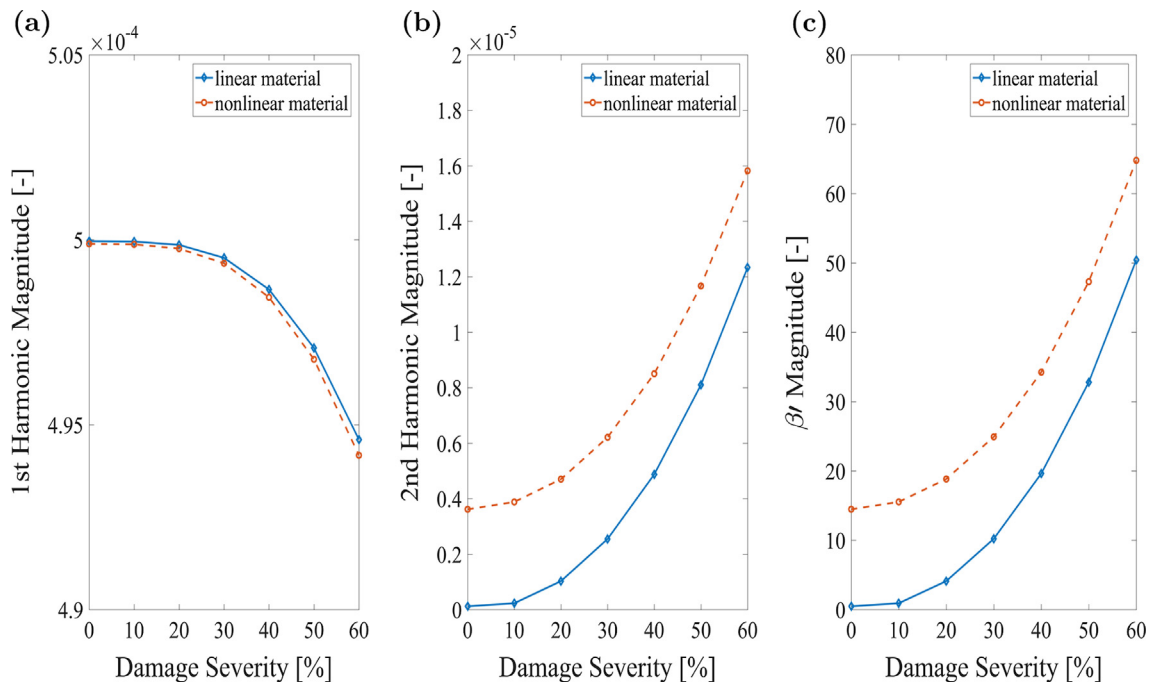


**Fig. 14.** Nonlinear Lamb wave parameters vs. damage severity for the linear and nonlinear material models: (a) First harmonic magnitude; (b) Second harmonic magnitude; (c)  $\beta'$  magnitude. The results were obtained for the S0–s0 mode pair and linear material model.

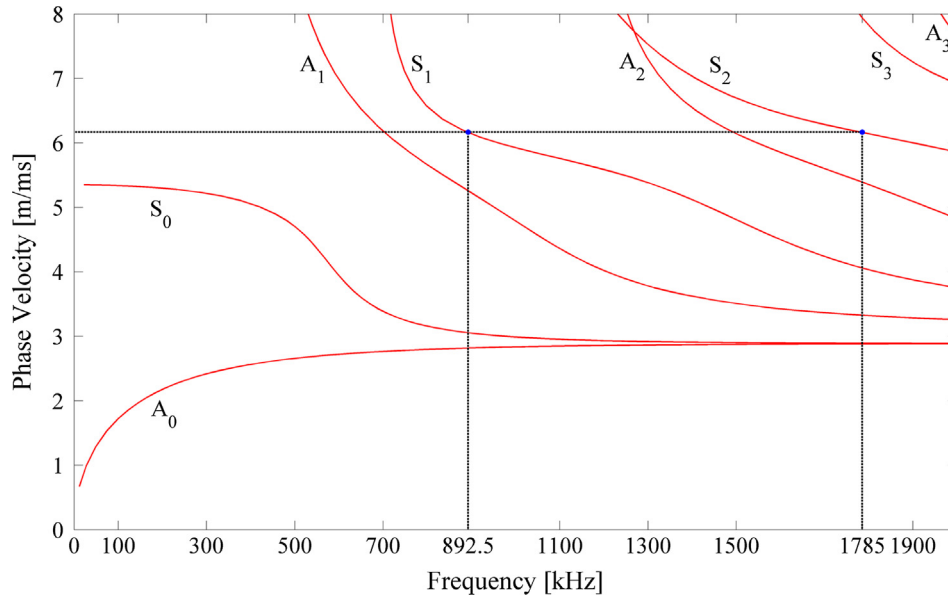


Fig. 15. Lamb wave dispersion curves for 4 mm thick aluminium beam used in numerical simulations.

characteristics – is not sufficient to extract amplitudes of the frequency components of interest. Thus, the Short-Time Fourier Transform (STFT) was applied to separate all modes and extract amplitudes of the  $S_1$  and  $s_2$  modes. Fig. 16 gives an example of the STFT plots for the responses collected 800 mm from the left hand side of the beam.

The results for the undamaged beam in Figs. 16a and c show that the second harmonic is generated only in the response for the beam with the nonlinear material. In contrast, when the beam is damaged the second harmonic  $s_2$  is exhibited for both – i.e. linear and nonlinear – material models and the amplitudes of this

harmonic are much stronger. Since the second harmonic can be generated also in the response from the undamaged beam (e.g. Fig. 16c), it is clear that in practice converted modes will also have to be analysed in order to detect damage.

By processing all of the collected signals with the use of STFT, the magnitude profiles in time domain are extracted at the frequencies of the particular interest, i.e. 892.5 kHz and 1.785 MHz (marked with dashed white line in Fig. 16). Due to the fact that at the chosen frequencies both  $S_1$  and  $s_2$  modes arrive first according to their dispersion characteristics, the maximum magnitudes of the first packages in the respective frequencies are obtained for all

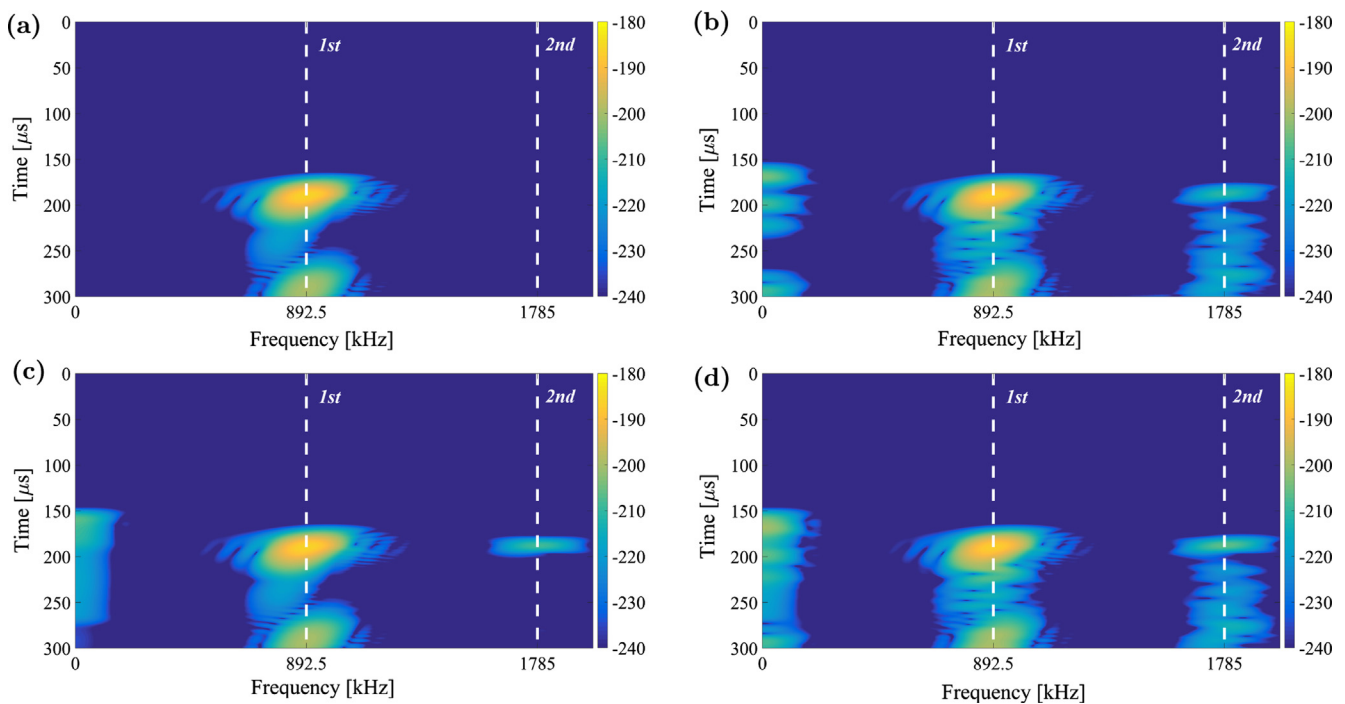


Fig. 16. Short Time Fourier Transform contour plots for the in-plane displacement signals captured at 800 mm from the left hand corner of the beam: (a) undamaged beam with the linear material model; (b) damaged beam (severity of damage equal to 20%) with the linear material model; (c) undamaged beam with the nonlinear material model; (d) damaged beam (severity of damage equal to 20%) with the nonlinear material model. Please note that contour plot magnitudes are plotted in a logarithmic scale.

damage and material definitions cases and are presented in propagation distance domain in Figs. 17 and 18. As in the previous section, the relative acoustic nonlinear parameter  $\beta'$  is also calculated and shown in the propagation distance domain.

Some interesting observation can be made when the reported magnitudes/parameters are analysed for different material models investigated. The results in Fig. 17b show that when the cracked beam is modelled using the linear material the second harmonic (mode s2) of the S1 mode is generated after the crack-wave interaction. This mode (second harmonic) continues to propagate in the beam and its amplitude remains relatively unchanged. Some amplitude increases in this case could be attributed to post-processing (i.e. magnitude extraction) of the contour plots with the use of STFT. These slight changes of magnitude could be considered as negligible if compared with the results given in Fig. 18b, where the same simulation results for the cracked beam were obtained using the nonlinear material model. Two sources of nonlinearity – i.e. “breathing” crack and material – generate the second harmonic with strongly increasing magnitudes over the wave propagation distance. The S1–s2 mode pair is synchronised also for the undamaged beam for which the magnitude of the second harmonic also increases with the propagation distance. However, the obtained magnitude growth trend is not linear. This observation can lead to the conclusion that the selected frequencies correspond rather to the approximate phase-velocity matching condition than to the exact phase-velocity matching, as explained in [28]. In other words, the analytical condition for synchronisation – defined in [26,28,36] – is met but not necessarily fulfilled by the numerical model. Previous result reported in [49,61] demonstrate that numerical dispersion characteristics strongly depend on mesh parameters. Therefore, even though numerical parameters satisfy stability conditions, it is possible that the numerical and analytical dispersion characteristics are different. As a result, even if the selected mode pair satisfies the analytical synchronisation condition, there is no guarantee that this condition will be met by the numerical model.

When the fundamental harmonic magnitude is analysed in Figs. 17a and 18a no significant difference can be observed in the reported plots. The magnitude of this harmonic decreases over

the wave propagation time for the linear and nonlinear model for all damage severities, as expected. The magnitude reduction is mainly due to the dispersion of the S1 mode and, in the case of models with nonlinear material, the energy transfer from the fundamental to the second harmonic s2 mode.

Finally, the relative acoustic nonlinear parameter  $\beta'$  exhibits some interesting features. Especially for the beam with the linear material model for which an increase of parameters' magnitude with the propagation distance can be noticed. This is not caused by the synchronisation condition of the S1–s2 mode pair, since the “breathing” crack is a local nonlinearity and the cumulative mechanism of magnitude increase over propagation distance does not apply in this case. This behaviour results rather from the steep magnitude decrease of the first harmonic that is highly dispersive if compared with second harmonic (see Fig. 15); the  $\beta'$  parameter is inversely proportional to the square of the first harmonic magnitude and not of much use for damage detection in this case. However, the usefulness of calculating the  $\beta'$  comes handy in the case of the models with nonlinear material and “breathing” crack. This conclusion is well depicted in the following figure. Similarly to the analysis performed in Section 5.1, Fig. 19 presents the values of all analysed parameters against damage severity.

First, attention should be directed to the results of the first harmonic characteristics (Fig. 19a), as the features of the second harmonic and the  $\beta'$  parameter require to be analysed together. It can be noticed that the first harmonic decreases in the domain of the crack size, which is commonly accepted feature when analysing the influence of the increasing size of the crack on the fundamental amplitude of the wave, i.e. wave attenuation. Moreover, it can be observed that the results from the models with nonlinear material have lower values than from the linear ones. It confirms the previously stated observation regarding the higher energy transfer to the second harmonic due to the presence of two sources of nonlinearity. On the other hand, a highly nonlinear dependence of the generated second harmonic (Fig. 19b) and the resulting parameter  $\beta'$  (Fig. 19c) magnitudes on the size of the “breathing” crack can be observed. One can notice that the second harmonic reaches its maximum values for the damage size equal to 30% of the beam thickness for the models with linear material and 20% for the beam

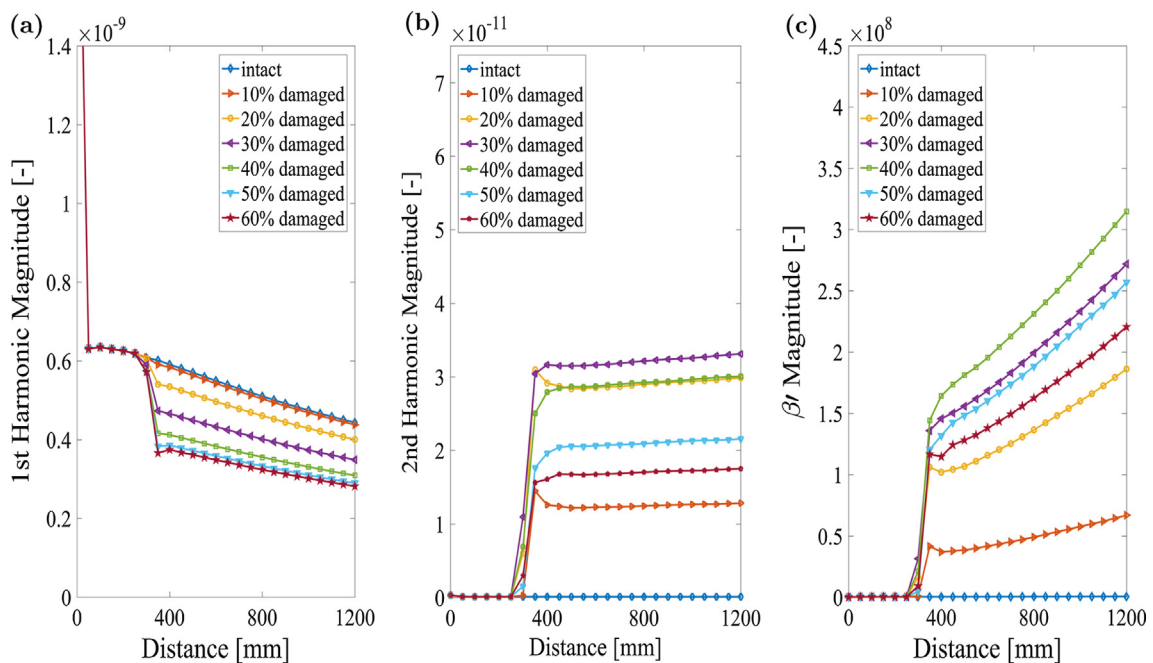
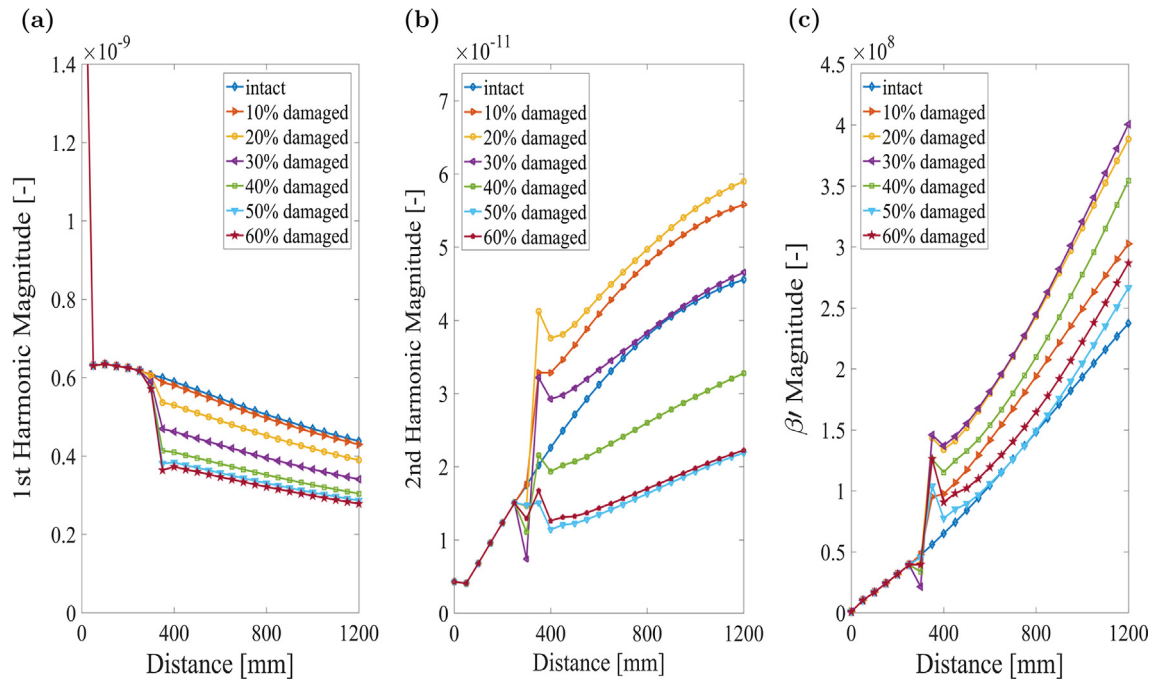
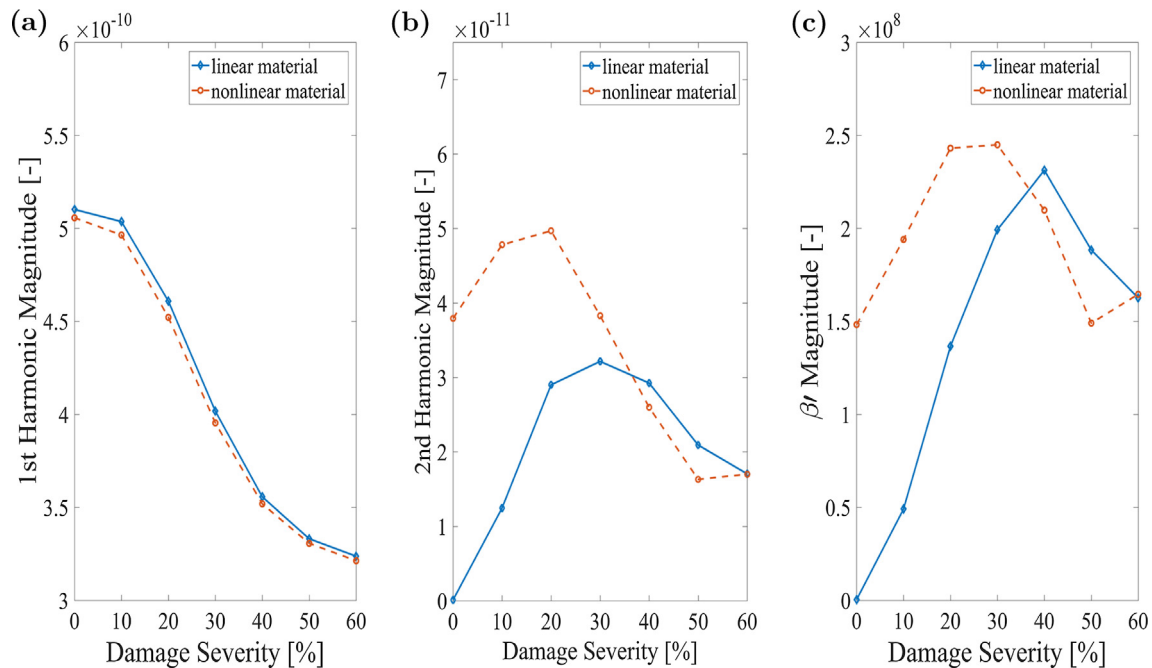


Fig. 17. Nonlinear parameters from undamaged and damaged beam models in the propagation distance domain: (a) First harmonic magnitude; (b) Second harmonic magnitude; (c)  $\beta'$  magnitude. The results were obtained for the S1–s2 mode pair and linear material model.



**Fig. 18.** Nonlinear parameters from undamaged and damaged beam models in the propagation distance domain: (a) First harmonic magnitude; (b) Second harmonic magnitude; (c)  $\beta'$  magnitude. The results were obtained for the S1–s2 mode pair and nonlinear material model.



**Fig. 19.** Nonlinear Lamb wave parameters vs. damage severity for the linear and nonlinear material models: (a) First harmonic magnitude; (b) Second harmonic magnitude; (c)  $\beta'$  magnitude. The results were obtained for the S1–s2 mode pair and linear material model.

with the nonlinear model. The second harmonic decreases with the size of the crack for larger crack depths. The nonlinear  $\beta'$  parameter reaches the maximum value for 40% and 30% crack depth, for linear and nonlinear material models, respectively. Hence, the S1–s2 mode pair is well suited to detect near–surface fatigue cracks, as concluded in previous research investigations [59,60]. As the crack depth increases, values of nonlinear parameters go down and as a result, damage detection becomes more difficult. This behaviour is in contrast to the S0–s0 mode pair, as demonstrated in Section 5.1. It can be noticed that for the S1–s2 mode pair the in-phase

summation between the second harmonics generated from the nonlinear material and “breathing” crack occur only when the cracks depth is between 0 and 20% of the beam thickness. For larger sizes of crack the second harmonics decreases, as a result of phase shift occurring between the respective second harmonic modes generated from two different sources. Such a difference in behaviour of the resultant second harmonic between the chosen mode pairs – i.e. S0–s0 mode pair and S1–s2 mode pair – is caused by the difference in complexity of the through–thickness mode shapes of s0 and s2 modes. The amplitude of the s0 mode is almost

uniformly distributed along the thickness, where the s2 mode has a trend of the cosine function along with the thickness. Thus, in-phase summation is more plausible to occur for S0–s0 mode pair than for S1–s2 mode pair, when two sources of nonlinearity are considered. Such outcome was also pointed out in [3].

### 5.3. Discussion

Interesting results are obtained from investigating the second harmonics generation in both low and high frequency range of the Lamb wave dispersion space. Both cases exhibit advantageous features which can be used in developing a NDE or SHM damage detection technique. The S0–s0 mode pair can be easily utilised to monitor the damage state of the structure, where the high frequency S1–s2 mode pair can be used to detect the embryo stages of the possible fatigue cracks in the examined structure.

Although, in the former case, a linear increase of the second harmonic magnitude is obtained from the analysis, one should be aware of the approximate phase velocity matching between the S0 and s0 modes. In the result, a beat-period will be observed in the much further propagation distance, as it was pointed out in [59]. Similar results were obtained in the presented paper, where the beat-period appears far beyond the area of investigation.

In the latter case, although the pair is considered as the one satisfying the “internal resonance”, an approximate behaviour is observed instead. One can see such an outcome as a certain flaw of the introduced numerical solution. However, having in mind an increasing number of investigations focused on monitoring the nonlinear aspects of the propagating wave using the numerical solutions [31,32,60], such a flaw has to be emphasized and appropriate steps should be taken in order to compensate them. Moreover, such compensation should not be reached in the domain of the excited frequency in order to achieve the “internal resonance” as the chosen parameter will be only applicable to the specific numerical approach (LISA, FEM, FDM, etc.) and will not be reflected in the different numerical solver or in the experiment. Therefore, the solution should be found in the defining new conditions for choosing the numerical parameters. First attempt to such parameters is shown in [58] and further steps should be taken in order to enhance the numerical modelling in the high frequency range of the Lamb wave dispersion curves.

## 6. Conclusions

Modelling and numerical simulation of nonlinear Lamb wave propagation in intact and cracked beams was investigated. The major focus was on the second harmonic generation caused by two sources of nonlinearity, i.e. the nonlinear hyper-elastic material and “breathing” crack. The cumulative effect of the second harmonic generated in the low (only basic Lamb wave modes) and high (higher-order Lamb wave modes) frequency range of Lamb wave dispersion curves were investigated. A new modelling tool based on NL–LISA and SM was proposed for all these tasks. The proposed model of crack involved a new condition for opening/closing the gap between the cracks interfaces. This condition was based on the normal stress evaluated between the cracks’ interfaces. The performance of the proposed NL–LISA/SM numerical tool was compared with the results based on the commercial FE ABAQUS® Software.

Numerical simulations based on NL–LISA/SM involved different material models (linear and nonlinear) and various severities of damage (crack depth). The magnitude of the second order harmonic generated by nonlinearities was investigated.

The simulation results demonstrate that the S0–s0 mode pair (low-frequency range) fulfils the approximate synchronisation condition and leads to cumulative second harmonic generation

when material is nonlinear. Further investigations reveal that this Lamb wave generation of this mode pair can be used to detect and monitor large crack severities. Moreover, when two sources of nonlinearity (i.e. material and damage) are present, with the increasing size of the crack material nonlinearity has less effect on the generated second harmonic.

The cumulative growth of the second harmonic mode was also observed when S1–s2 mode pair (high-frequency range) was used for nonlinear Lamb wave propagation. The results demonstrated that the S1–s2 mode pair is better suited to detect smaller crack depths. The “internal resonance” – required for the synchronisation condition to achieve a linear growth of the second harmonic magnitude – was met only approximately for this mode pair, leading to some discrepancies with respect to the magnitude behaviour. This is mainly due to numerical conditions that are important to obtain good quality dispersion characteristics. Further research work is required to investigate this problem.

Nevertheless, both synchronous mode pairs investigated offer good potential for damage detection based on nonlinear Lamb wave propagation. It is anticipated that the proposed numerical simulation platform – based on NL–LISA and SM – will contribute to further developments in this field, leading to new reliable nonlinear damage detection methods. Further experimental investigations should also be performed to confirm the observed phenomena.

## Appendix A. Nonlinear stress–displacement equations

$$\begin{aligned}
 T_{xx} = & (\lambda + 2\mu) \left( \frac{\partial u}{\partial x} + \frac{1}{2} \left( \frac{\partial u}{\partial x} \right)^2 + \frac{1}{2} \left( \frac{\partial v}{\partial x} \right)^2 \right) \\
 & + \lambda \left( \frac{\partial v}{\partial y} + \frac{1}{2} \left( \frac{\partial u}{\partial y} \right)^2 + \frac{1}{2} \left( \frac{\partial v}{\partial y} \right)^2 \right) \\
 & + (\mathcal{A} + 3\mathcal{B} + \mathcal{C}) \left( \left( \frac{\partial u}{\partial x} \right)^2 + \left( \frac{\partial u}{\partial x} \right)^3 + \frac{\partial u}{\partial x} \left( \frac{\partial v}{\partial x} \right)^2 \right) \\
 & + \frac{1}{2} \left( \frac{\partial u}{\partial x} \right)^2 \left( \frac{\partial u}{\partial x} \right)^2 + \frac{1}{4} \left( \frac{\partial u}{\partial x} \right)^4 + \frac{1}{4} \left( \frac{\partial v}{\partial x} \right)^4 \\
 & + (\mathcal{B} + \mathcal{C}) \left( \left( \frac{\partial v}{\partial y} \right)^2 + \left( \frac{\partial v}{\partial y} \right)^3 + \frac{\partial v}{\partial y} \left( \frac{\partial u}{\partial y} \right)^2 \right) \\
 & + \frac{1}{2} \left( \frac{\partial u}{\partial y} \right)^2 \left( \frac{\partial v}{\partial y} \right)^2 + \frac{1}{4} \left( \frac{\partial u}{\partial y} \right)^4 + \frac{1}{4} \left( \frac{\partial v}{\partial y} \right)^4 \\
 & + (2\mathcal{B} + 2\mathcal{C}) \left( \frac{\partial u}{\partial x} \frac{\partial v}{\partial y} + \frac{1}{2} \frac{\partial u}{\partial x} \left( \frac{\partial u}{\partial y} \right)^2 + \frac{1}{2} \frac{\partial u}{\partial x} \left( \frac{\partial v}{\partial y} \right)^2 \right) \\
 & + \frac{1}{2} \frac{\partial v}{\partial y} \left( \frac{\partial u}{\partial x} \right)^2 + \frac{1}{2} \frac{\partial v}{\partial y} \left( \frac{\partial v}{\partial x} \right)^2 \\
 & + \frac{1}{4} \left( \frac{\partial u}{\partial x} \right)^2 \left( \frac{\partial u}{\partial y} \right)^2 + \frac{1}{4} \left( \frac{\partial u}{\partial x} \right)^2 \left( \frac{\partial v}{\partial y} \right)^2 \\
 & + \frac{1}{4} \left( \frac{\partial u}{\partial y} \right)^2 \left( \frac{\partial v}{\partial x} \right)^2 + \frac{1}{4} \left( \frac{\partial v}{\partial x} \right)^2 \left( \frac{\partial v}{\partial y} \right)^2 \\
 & + (\mathcal{A} + 2\mathcal{B}) \left( \frac{1}{4} \left( \frac{\partial u}{\partial y} \right)^2 + \frac{1}{2} \frac{\partial u}{\partial y} \frac{\partial v}{\partial x} + \frac{1}{4} \left( \frac{\partial v}{\partial x} \right)^2 \right) \\
 & + \frac{1}{2} \frac{\partial u}{\partial x} \left( \frac{\partial u}{\partial y} \right)^2 + \frac{1}{2} \frac{\partial u}{\partial x} \frac{\partial u}{\partial y} \frac{\partial v}{\partial x} + \frac{1}{2} \frac{\partial u}{\partial y} \frac{\partial v}{\partial x} \frac{\partial v}{\partial y} \\
 & + \frac{1}{2} \frac{\partial v}{\partial y} \left( \frac{\partial v}{\partial x} \right)^2 + \frac{1}{4} \left( \frac{\partial u}{\partial x} \right)^2 \left( \frac{\partial u}{\partial y} \right)^2 \\
 & + \frac{1}{2} \frac{\partial u}{\partial x} \frac{\partial u}{\partial y} \frac{\partial v}{\partial x} \frac{\partial v}{\partial y} + \frac{1}{4} \left( \frac{\partial v}{\partial x} \right)^2 \left( \frac{\partial v}{\partial y} \right)^2
 \end{aligned} \tag{A.1}$$

$$\begin{aligned}
T_{yy} = & (\lambda + 2\mu) \left( \frac{\partial v}{\partial y} + \frac{1}{2} \left( \frac{\partial u}{\partial y} \right)^2 + \frac{1}{2} \left( \frac{\partial v}{\partial y} \right)^2 \right) \\
& + \lambda \left( \frac{\partial u}{\partial x} + \frac{1}{2} \left( \frac{\partial u}{\partial x} \right)^2 + \frac{1}{2} \left( \frac{\partial v}{\partial x} \right)^2 \right) \\
& + (\mathcal{A} + 3\mathcal{B} + \mathcal{C}) \left( \left( \frac{\partial v}{\partial y} \right)^2 + \left( \frac{\partial v}{\partial y} \right)^3 + \frac{\partial u}{\partial y} \left( \frac{\partial u}{\partial y} \right)^2 \right) \\
& + \frac{1}{2} \left( \frac{\partial u}{\partial y} \right)^2 \left( \frac{\partial v}{\partial y} \right)^2 + \frac{1}{4} \left( \frac{\partial u}{\partial y} \right)^4 + \frac{1}{4} \left( \frac{\partial v}{\partial y} \right)^4 \\
& + (\mathcal{B} + \mathcal{C}) \left( \left( \frac{\partial u}{\partial x} \right)^2 + \left( \frac{\partial u}{\partial x} \right)^3 + \frac{\partial u}{\partial x} \left( \frac{\partial v}{\partial x} \right)^2 \right) \\
& + \frac{1}{2} \left( \frac{\partial u}{\partial x} \right)^2 \left( \frac{\partial v}{\partial x} \right)^2 + \frac{1}{4} \left( \frac{\partial u}{\partial x} \right)^4 + \frac{1}{4} \left( \frac{\partial v}{\partial x} \right)^4 \\
& + (2\mathcal{B} + 2\mathcal{C}) \left( \frac{\partial u}{\partial x} \frac{\partial v}{\partial y} + \frac{1}{2} \frac{\partial u}{\partial x} \left( \frac{\partial u}{\partial y} \right)^2 + \frac{1}{2} \frac{\partial u}{\partial x} \left( \frac{\partial v}{\partial y} \right)^2 \right) \\
& + \frac{1}{2} \frac{\partial v}{\partial y} \left( \frac{\partial u}{\partial x} \right)^2 + \frac{1}{2} \frac{\partial v}{\partial y} \left( \frac{\partial v}{\partial x} \right)^2 \\
& + \frac{1}{4} \left( \frac{\partial u}{\partial x} \right)^2 \left( \frac{\partial u}{\partial y} \right)^2 + \frac{1}{4} \left( \frac{\partial u}{\partial x} \right)^2 \left( \frac{\partial v}{\partial y} \right)^2 \\
& + \frac{1}{4} \left( \frac{\partial u}{\partial y} \right)^2 \left( \frac{\partial v}{\partial x} \right)^2 + \frac{1}{4} \left( \frac{\partial v}{\partial x} \right)^2 \left( \frac{\partial v}{\partial y} \right)^2 \\
& + (\mathcal{A} + 2\mathcal{B}) \left( \frac{1}{4} \left( \frac{\partial u}{\partial y} \right)^2 + \frac{1}{2} \frac{\partial u}{\partial y} \frac{\partial v}{\partial x} + \frac{1}{4} \left( \frac{\partial v}{\partial x} \right)^2 \right) \\
& + \frac{1}{2} \frac{\partial u}{\partial x} \left( \frac{\partial u}{\partial y} \right)^2 + \frac{1}{2} \frac{\partial u}{\partial x} \frac{\partial u}{\partial y} \frac{\partial v}{\partial x} + \frac{1}{2} \frac{\partial u}{\partial y} \frac{\partial v}{\partial x} \frac{\partial v}{\partial y} \\
& + \frac{1}{2} \frac{\partial v}{\partial y} \left( \frac{\partial v}{\partial x} \right)^2 + \frac{1}{4} \left( \frac{\partial u}{\partial x} \right)^2 \left( \frac{\partial u}{\partial y} \right)^2 \\
& + \frac{1}{2} \frac{\partial u}{\partial x} \frac{\partial u}{\partial y} \frac{\partial v}{\partial x} \frac{\partial v}{\partial y} + \frac{1}{4} \left( \frac{\partial v}{\partial x} \right)^2 \left( \frac{\partial v}{\partial y} \right)^2
\end{aligned} \tag{A.2}$$

$$\begin{aligned}
T_{xy} = & \mu \left( \frac{\partial u}{\partial y} + \frac{\partial v}{\partial x} + \frac{\partial u}{\partial x} \frac{\partial u}{\partial y} + \frac{\partial v}{\partial x} \frac{\partial v}{\partial y} \right) \\
& + (\mathcal{A} + 2\mathcal{B}) \left( \frac{1}{2} \frac{\partial u}{\partial x} \frac{\partial u}{\partial y} + \frac{1}{2} \frac{\partial u}{\partial x} \frac{\partial v}{\partial x} + \frac{3}{4} \frac{\partial u}{\partial y} \left( \frac{\partial u}{\partial x} \right)^2 \right) \\
& + \frac{1}{4} \frac{\partial u}{\partial y} \left( \frac{\partial u}{\partial x} \right)^3 + \frac{1}{4} \frac{\partial v}{\partial x} \left( \frac{\partial u}{\partial x} \right)^2 + \frac{1}{4} \frac{\partial u}{\partial y} \left( \frac{\partial v}{\partial x} \right)^2 \\
& + \frac{1}{4} \frac{\partial v}{\partial y} \left( \frac{\partial v}{\partial x} \right)^3 + \frac{1}{4} \left( \frac{\partial v}{\partial x} \right)^3 + \frac{1}{4} \frac{\partial u}{\partial x} \frac{\partial u}{\partial y} \left( \frac{\partial v}{\partial x} \right)^2 \\
& + \frac{1}{4} \frac{\partial v}{\partial x} \frac{\partial v}{\partial y} \left( \frac{\partial u}{\partial x} \right)^2 + \frac{1}{2} \frac{\partial u}{\partial x} \frac{\partial v}{\partial x} \frac{\partial v}{\partial y} \\
& + (\mathcal{A} + 2\mathcal{B}) \left( \frac{1}{2} \frac{\partial u}{\partial y} \frac{\partial v}{\partial y} + \frac{1}{2} \frac{\partial v}{\partial x} \frac{\partial v}{\partial y} + \frac{3}{4} \frac{\partial v}{\partial x} \left( \frac{\partial v}{\partial y} \right)^2 \right) \\
& + \frac{1}{4} \frac{\partial u}{\partial x} \left( \frac{\partial u}{\partial y} \right)^3 + \frac{1}{4} \frac{\partial v}{\partial x} \left( \frac{\partial u}{\partial y} \right)^2 + \frac{1}{4} \frac{\partial u}{\partial y} \left( \frac{\partial v}{\partial y} \right)^2 \\
& + \frac{1}{4} \frac{\partial v}{\partial x} \left( \frac{\partial v}{\partial y} \right)^3 + \frac{1}{4} \left( \frac{\partial u}{\partial y} \right)^3 + \frac{1}{4} \frac{\partial u}{\partial x} \frac{\partial u}{\partial y} \left( \frac{\partial v}{\partial y} \right)^2 \\
& + \frac{1}{4} \frac{\partial v}{\partial x} \frac{\partial v}{\partial y} \left( \frac{\partial u}{\partial y} \right)^2 + \frac{1}{2} \frac{\partial u}{\partial x} \frac{\partial u}{\partial y} \frac{\partial v}{\partial y}
\end{aligned} \tag{A.3}$$

## References

- [1] C. Zhou, Z. Su, L. Cheng, Quantitative evaluation of orientation-specific damage using elastic waves and probability-based diagnostic imaging, *Mech. Syst. Sign. Process.* 25 (6) (2011) 2135–2156, <https://doi.org/10.1016/j.ymssp.2011.02.001>. <<http://www.sciencedirect.com/science/article/pii/S088832701100063X>>.
- [2] G.P. Malfense Fierro, F. Ciampa, D. Ginzburg, E. Onder, M. Meo, Nonlinear ultrasound modelling and validation of fatigue damage, *J. Sound Vib.* 343 (2015) 121–130.
- [3] V.K. Chillara, C.J. Lissenden, Nonlinear guided waves in plates undergoing localized microstructural changes, *AIP Conf. Proc.* 1650 (1) (2015) 1561–1569, <https://doi.org/10.1063/1.4914775>. <<http://aip.scitation.org/doi/abs/10.1063/1.4914775>>.
- [4] M. Destrade, R.W. Ogden, On the third- and fourth-order constants of incompressible isotropic elasticity, *J. Acoust. Soc. Am.* 128 (6) (2010) 3334–3343.
- [5] A. Khashtarash, R. Hassannejad, Energy dissipation caused by fatigue crack in beam-like cracked structures, *J. Sound Vib.* 36 (2016) 247–257.
- [6] Y.K. An, H. Sohn, Visualization of non-propagating Lamb wave modes for fatigue crack evaluation, *J. Appl. Phys.* 117 (11) (2015) 114904, <https://doi.org/10.1063/1.4906499>.
- [7] Z. Lv, H.-Z. Huang, S.-P. Zhu, H. Gao, F. Zuo, A modified nonlinear fatigue damage accumulation model, *Int. J. Damage Mech.* 24 (2) (2015) 168–181, <https://doi.org/10.1177/1056789514524075>.
- [8] G. Shui, Y.S. Wang, P. Huang, J. Qu, Nonlinear ultrasonic evaluation of the fatigue damage of adhesive joints, *NDT&E Int.* 70 (2015) 9–15.
- [9] A. Guha, C.R. Bjudas, Higher and sub-harmonic Lamb wave mode generation due to debond-induced contact nonlinearity, *Proc. SPIE* 9805 (2016), 98050X–98050X–20.
- [10] G. Scarselli, F. Ciampa, D. Ginzburg, M. Meo, Non-destructive testing techniques based on nonlinear methods for assessment of debonding in single lap joints, *Proc. SPIE* 9437 (2015), 943706–943706–11.
- [11] M. Hong, Z. Su, Q. Wang, L. Cheng, X. Qing, Modeling nonlinearities of ultrasonic waves for fatigue damage characterization: theory, simulation, and experimental validation, *Ultrasonics* 54 (3) (2014) 770–778.
- [12] C.J. Lissenden, Y. Liu, G.W. Choi, X. Yao, Effect of localized microstructure evolution on higher harmonic generation of guided waves, *J. Nondestruct. Eval.* 33 (2) (2014) 178–186.
- [13] G. Choi, Y. Liu, X. Yao, C.J. Lissenden, Effect of localized microstructural evolution on higher harmonic generation of guided wave modes, *AIP Conf. Proc.* 1650 (1) (2015) 1592–1598.
- [14] V.K. Chillara, C.J. Lissenden, Nonlinear guided waves in plates: a numerical perspective, *Ultrasonics* 54 (6) (2014) 1553–1558.
- [15] D. Dutta, H. Sohn, K.A. Harries, P. Rizzo, A nonlinear acoustic technique for crack detection in metallic structures, *Struct. Health Monit.* 8 (3) (2009) 251–262.
- [16] M. Deng, Analysis of second-harmonic generation of Lamb modes using a modal analysis approach, *J. Appl. Phys.* 94 (6) (2003) 4152–4159.
- [17] C. Zhou, M. Hong, Z. Su, Q. Wang, L. Cheng, Evaluation of fatigue cracks using nonlinearities of acousto-ultrasonic waves acquired by an active sensor network, *Smart Mater. Struct.* 22 (1) (2013) 015018. <<http://stacks.iop.org/0964-1726/22/i=1/a=015018>>.
- [18] I. Solodov, J. Wackerl, K. Pfeleiderer, G. Busse, Nonlinear self-modulation and subharmonic acoustic spectroscopy for damage detection and location, *Appl. Phys. Lett.* 84 (26) (2004) 5386–5388.
- [19] F. Aymerich, W.J. Staszewski, Experimental study of impact-damage detection in composite laminates using a cross-modulation vibro-acoustic technique, *Struct. Health Monit.* 9 (6) (2010) 541–553.
- [20] M. Muller, A. Sutin, R. Guyer, M. Talmant, P. Laugier, P.A. Johnson, Nonlinear resonant ultrasound spectroscopy (NRUS) applied to damage assessment in bone, *J. Acoust. Soc. Am.* 118 (6) (2005) 3946–3952.
- [21] D.T. Zeitvogel, K.H. Matlack, J.Y. Kim, L.J. Jacobs, P.M. Singh, J. Qu, Characterization of stress corrosion cracking in carbon steel using nonlinear Rayleigh surface waves, *NDT&E Int.* 62 (2014) 144–152.
- [22] J.-Y. Kim, V.A. Yakovlev, S.I. Rokhlin, Parametric modulation mechanism of surface acoustic wave on a partially closed crack, *Appl. Phys. Lett.* 82 (19) (2003) 3203–3205.
- [23] T. Stratoudaki, R. Ellwood, S. Sharples, M. Clark, M.G. Somekh, I.J. Collison, Measurement of material nonlinearity using surface acoustic wave parametric interaction and laser ultrasonics, *J. Acoust. Soc. Am.* 129 (4) (2011) 1721–1728.
- [24] J. Riviere, S. Hauptert, P. Laugier, T. Ulrich, P.-Y. Le Bas, P. Johnson, Time reversed elastic nonlinearity diagnostic applied to mock osseointegration monitoring applying two experimental models, *J. Acoust. Soc. Am.* 131 (3) (2012) 1922–1927.
- [25] K.-Y. Jhang, Nonlinear ultrasonic techniques for nondestructive assessment of micro damage in material: a review, *Int. J. Precis. Eng. Manuf.* 10 (1) (2009) 123–135.
- [26] M. Deng, Cumulative second-harmonic generation of Lamb-mode propagation in a solid plate, *J. Appl. Phys.* 85 (6) (1999) 3051–3058.
- [27] W.J.N. de Lima, M.F. Hamilton, Finite-amplitude waves in isotropic elastic plates, *J. Sound Vib.* 265 (4) (2003) 819–839.
- [28] M.F. Müller, J.-Y. Kim, J. Qu, L.J. Jacobs, Characteristics of second harmonic generation of Lamb waves in nonlinear elastic plates, *J. Acoust. Soc. Am.* 127 (4) (2010) 2141–2152.

- [29] N. Matsuda, S. Biwa, Phase and group velocity matching for cumulative harmonic generation in Lamb waves, *J. Appl. Phys.* 109 (9) (2011) 094903, <https://doi.org/10.1063/1.3569864>.
- [30] A.S. Gliozzi, M. Scalerandi, Modeling dynamic acousto-elastic testing experiments: validation and perspectives, *J. Acoust. Soc. Am.* 136 (4) (2014) 1530–1541.
- [31] N. Rauter, R. Lammering, Numerical simulation of elastic wave propagation in isotropic media considering material and geometrical nonlinearities, *Smart Mater. Struct.* 24 (4) (2015) 045027.
- [32] Y. Shen, C.E.S. Cesnik, Modeling of nonlinear interactions between guided waves and fatigue cracks using local interaction simulation approach, *Ultrasonics* 74 (2017) 106–123, <https://doi.org/10.1016/j.ultras.2016.10.001>. <<http://www.sciencedirect.com/science/article/pii/S0041624X16302049>>.
- [33] P. Zuo, Y. Zhou, Z. Fan, Numerical studies of nonlinear ultrasonic guided waves in uniform waveguides with arbitrary cross sections, *AlP Adv.* 6 (7) (2016) 075207, <https://doi.org/10.1063/1.4959005>.
- [34] M. Deng, P. Wang, X. Lv, Experimental verification of cumulative growth effect of second harmonics of Lamb wave propagation in an elastic plate, *Appl. Phys. Lett.* 86 (12) (2005) 124104, <https://doi.org/10.1063/1.1891295>.
- [35] K.H. Matlack, J.Y. Kim, L.J. Jacobs, J. Qu, Experimental characterization of efficient second harmonic generation of lamb wave modes in a nonlinear elastic isotropic plate, *J. Appl. Phys.* 109 (1) (2011) 014905, <https://doi.org/10.1063/1.3527959>.
- [36] Y. Liu, V.K. Chhillara, C.J. Lissenden, On selection of primary modes for generation of strong internally resonant second harmonics in plate, *J. Sound Vib.* 332 (19) (2013) 4517–4528.
- [37] P. Zuo, Y. Zhou, Z. Fan, Numerical and experimental investigation of nonlinear ultrasonic lamb waves at low frequency, *Appl. Phys. Lett.* 109 (2) (2016) 021902, <https://doi.org/10.1063/1.4958705>.
- [38] P.P. Delsanto, T. Whitcombe, H.H. Chaskelis, R.B. Mignogna, Connection machine simulation of ultrasonic wave propagation in materials. I: The one-dimensional case, *Wave Motion* 16 (1) (1992) 65–80.
- [39] P.P. Delsanto, R.S. Schechter, H.H. Chaskelis, R.B. Mignogna, R. Kline, Connection machine simulation of ultrasonic wave propagation in materials. II: The two-dimensional case, *Wave Motion* 20 (4) (1994) 295–314.
- [40] P.P. Delsanto, R.S. Schechter, R.B. Mignogna, Connection machine simulation of ultrasonic wave propagation in materials III: The three-dimensional case, *Wave Motion* 26 (4) (1997) 329–339.
- [41] P. Packo, T. Bielak, A.B. Spencer, T. Uhl, W.J. Staszewski, K. Worden, T. Barszcz, P. Russek, K. Wiatr, Numerical simulations of elastic wave propagation using graphical processing units – comparative study of high-performance computing capabilities, *Comput. Methods Appl. Mech. Eng.* 290 (2015) 98–126.
- [42] M.B. Obenchain, K.S. Nadella, C.E.S. Cesnik, Hybrid global matrix/local interaction simulation approach for wave propagation in composites, *AIAA J.* 53 (2) (2015) 379–393.
- [43] K.S. Nadella, C.E.S. Cesnik, Local interaction simulation of guided-wave propagation in composite plate using CloVER transducer, in: *Structural Health Monitoring 2011: Condition-Based Maintenance and Intelligent Structures – Proceedings of the 8th International Workshop on Structural Health Monitoring*, vol. 2, 2011, pp. 2529–2536.
- [44] L. Borkowski, K. Liu, A. Chattopadhyay, Fully coupled electromechanical elastodynamic model for guided wave propagation analysis, *J. Intell. Mater. Syst. Struct.* 24 (13) (2013) 1647–1663.
- [45] S. Sundararaman, D.E. Adams, Accuracy and convergence using a local interaction simulation approach in one, two, and three dimensions, *J. Appl. Mech.* 76 (3) (2009), 031008–031008–10.
- [46] B.C. Lee, W.J. Staszewski, Lamb wave propagation modelling for damage detection: I. Two-dimensional analysis, *Smart Mater. Struct.* 16 (2) (2007) 249.
- [47] B.C. Lee, W.J. Staszewski, Lamb wave propagation modelling for damage detection: II. Damage monitoring strategy, *Smart Mater. Struct.* 16 (2) (2007) 260. <<http://stacks.iop.org/0964-1726/16/i=2/a=004>>.
- [48] M.B. Obenchain, C.E.S. Cesnik, Guided wave interaction with hole damage using the local interaction simulation approach, *Smart Mater. Struct.* 23 (12) (2014) 125010.
- [49] R. Radecki, M.J. Leamy, T. Uhl, W.J. Staszewski, Z. Su, L. Cheng, P. Packo, Investigation on high-order harmonic generation of guided waves using local computation approaches: theory and comparison with analytical modelling, in: *EWSHM-7th European Workshop on Structural Health Monitoring*, 2014.
- [50] M.J. Leamy, T.B. Atrusson, W.J. Staszewski, T. Uhl, P. Packo, Local computational strategies for predicting wave propagation in nonlinear media, *Proc. SPIE* 9064 (2014), <https://doi.org/10.1117/12.2045041>, 90641J–90641J–15.
- [51] P.P. Delsanto, M. Scalerandi, A spring model for the simulation of the propagation of ultrasonic pulses through imperfect contact interfaces, *J. Acoust. Soc. Am.* 104 (5) (1998) 2584–2591.
- [52] L.D. Landau, E.M. Lifshitz, *Theory of Elasticity*, second ed., Pergamon Press, 1970.
- [53] P. Packo, T. Bielak, A.B. Spencer, W.J. Staszewski, T. Uhl, K. Worden, Lamb wave propagation modelling and simulation using parallel processing architecture and graphical cards, *Smart Mater. Struct.* 21 (7) (2012) 075001.
- [54] R. Radecki, An Insight into Nonlinearity of Guided Ultrasonic Waves in Fatigued Materials based on a Nonlinear Local Interaction Simulation Approach: Theory, Modelling and Experimental Validation, Ph.D. thesis, The Hong Kong Polytechnic University, 2016.
- [55] D. Broda, W.J. Staszewski, A. Martowicz, T. Uhl, V.V. Silberschmidt, Modelling of nonlinear crack-wave interactions for damage detection based on ultrasound – a review, *J. Sound Vib.* 333 (4) (2014) 1097–1118.
- [56] R.F.S. Hearmon, The third- and higher-order elastic constants, in: K.H. Hellwege, A.M. Hellwege (Eds.), *Elastic, Piezoelectric, Pyroelectric, Piezooptic, Electrooptic Constants, and Nonlinear Dielectric Susceptibilities of Crystals*, vol. III/11, Landolt-Börnstein, New Series, Springer, New York, 1979, pp. 109–308.
- [57] Y. Shen, V. Giurgiutiu, Predictive modeling of nonlinear wave propagation for structural health monitoring with piezoelectric wafer active sensors, *J. Intell. Mater. Syst. Struct.* 25 (4) (2014) 506–520.
- [58] P. Packo, T. Uhl, W.J. Staszewski, M.J. Leamy, Amplitude-dependent lamb wave dispersion in nonlinear plates, *J. Acoust. Soc. Am.* 140 (2) (2016) 1319–1331, <https://doi.org/10.1121/1.4961489>.
- [59] X. Wan, P.W. Tse, G.H. Xu, T.F. Tao, Q. Zhang, Analytical and numerical studies of approximate phase velocity matching based nonlinear s0 mode lamb waves for the detection of evenly distributed microstructural changes, *Smart Mater. Struct.* 25 (4) (2016) 045023.
- [60] V.K. Chhillara, C.J. Lissenden, Review of nonlinear ultrasonic guided wave nondestructive evaluation: theory, numerics and experiments, *Opt. Eng.* 55 (1) (2015).
- [61] P. Packo, T. Uhl, W.J. Staszewski, Generalized semi-analytical finite difference method for dispersion curves calculation and numerical dispersion analysis for Lamb waves, *J. Acoust. Soc. Am.* 136 (3) (2014) 993–1002.